Sparsely Pillared Graphene Materials for High-Performance Supercapacitors: Improving Ion Transport and Storage Capacity

Harish Banda, Sandy Périé, Barbara Daffos, Pierre-Louis Taberna, Lionel Dubois, Olivier Crosnier, Patrice Simon, Daniel Lee, Gaël de Paëpe, Florence Duclairoir

To cite this version:

Banda, Harish and Périé, Sandy and Daffos, Barbara and Taberna, Pierre-Louis and Dubois, Lionel and Crosnier, Olivier and Simon, Patrice and Lee, Daniel and De Paëpe, Gaël and Duclairoir, Florence *Sparsely Pillared Graphene Materials for High-Performance Supercapacitors: Improving Ion Transport and Storage Capacity.* (2019) ACS Nano, 13 (2). 1443-1453. ISSN 1936-0851

Sparsely Pillared Graphene Materials for High-Performance Supercapacitors: Improving Ion Transport and Storage Capacity

Harish Banda,[†] Sandy Périé,[†] Barbara Daffos,[‖,‡] Pierre-Louis Taberna,[‖,‡] Lionel Dubois,[†] Olivier Crosnier,[‖,§] Patrice Simon,[‖,‡] Daniel Lee,[†] Gaël De Paëpe,[†] and Florence Duclairoir*[†]

[†]Université Grenoble Alpes, CEA, CNRS, INAC, Grenoble 38000, France
[‡]CIRIMAT, Université de Toulouse, CNRS, INPT, UPS, Toulouse 31062, France
[§]Institut des Matériaux Jean Rouxel (IMN), Université de Nantes, CNRS, Nantes 44300, France
[‖]Réseau sur le Stockage Electrochimique de l'Energie (RS2E), CNRS FR3459, Amiens 80039, France

● *Supporting Information*
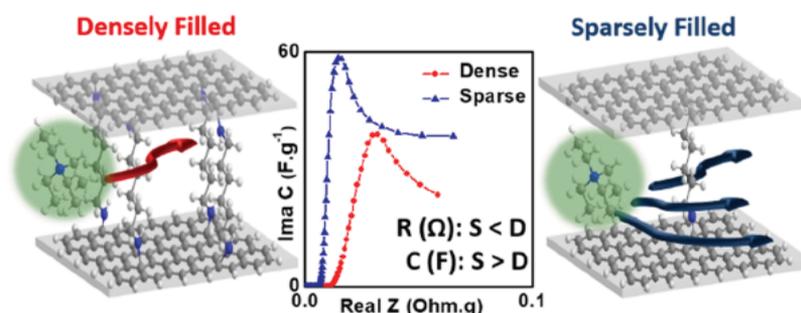
**ABSTRACT:** Graphene based materials are extensively studied as promising candidates for supercapacitors (SCs) owing to the high surface area, electrical conductivity, and mechanical flexibility of graphene. Reduced graphene oxide (RGO), a close graphene like material studied for SCs, offers limited specific capacitances ($100 \, F \cdot g^{-1}$) as the reduced graphene sheets partially restack through $\pi-\pi$ interactions. This paper presents pillared graphene materials designed to minimize such graphitic restacking by cross linking the graphene sheets with a bifunctional pillar molecule. Solid state NMR, X ray diffraction, and electrochemical analyses reveal that the synthesized materials possess covalently cross linked graphene galleries that offer additional sites for ion sorption in SCs. Indeed, high specific capacitances in SCs are observed for the graphene materials synthesized with an optimized number of pillars. Specifically, the straightforward synthesis of a graphene hydrogel containing pillared structures and an interconnected porous network delivered a material with gravimetric capacitances two times greater than that of RGO ($200 \, F \cdot g^{-1}$ *vs* $107 \, F \cdot g^{-1}$) and volumetric capacitances that are nearly four times larger ($210 \, F \cdot cm^{-3}$ *vs* $54 \, F \cdot cm^{-3}$). Additionally, despite the presence of pillars inside the graphene galleries, the optimized materials show efficient ion transport characteristics. This work therefore brings perspectives for the next generation of high performance SCs.

KEYWORDS: *supercapacitors, pillared graphene, ion sieving, graphene hydrogel, interlayer galleries*

Electrochemical double layer capacitors (EDLC), also known as supercapacitors (SCs), are devices that store energy through charge separation from electrolytic ion sorption on charged electrode surfaces.[1] There is a huge interest in developing improved SCs owing to the urgent need for efficient energy storage devices in mobile applications.[2] Porous carbons such as activated carbons (ACs) are traditionally used as electrode materials due to their high surface areas and low costs.[3,4] In the past decade, important capacitance contributions from micropores in carbon materials were discovered in ACs and carbide derived carbons (CDCs).[5−7]

Ultramicropores (<1 nm) that were previously thought to be inaccessible for electrolytic ions exhibit significant ion sorption capabilities.[2,8] Extensive studies on materials with tailored pores sizes have revealed that the electrolytic ions partially desolvate and access pores that are otherwise too small to be accessible.[9,10] Further analyses using modeling[11] and *in situ*[12−15] and *ex situ* techniques[16] have shown that the

Scheme 1. Synthesis of Reduced Pillared Graphene Materials (RPs) and Pillared Graphene Hydrogels (GHs) using 1,6 Diaminohexane[a]
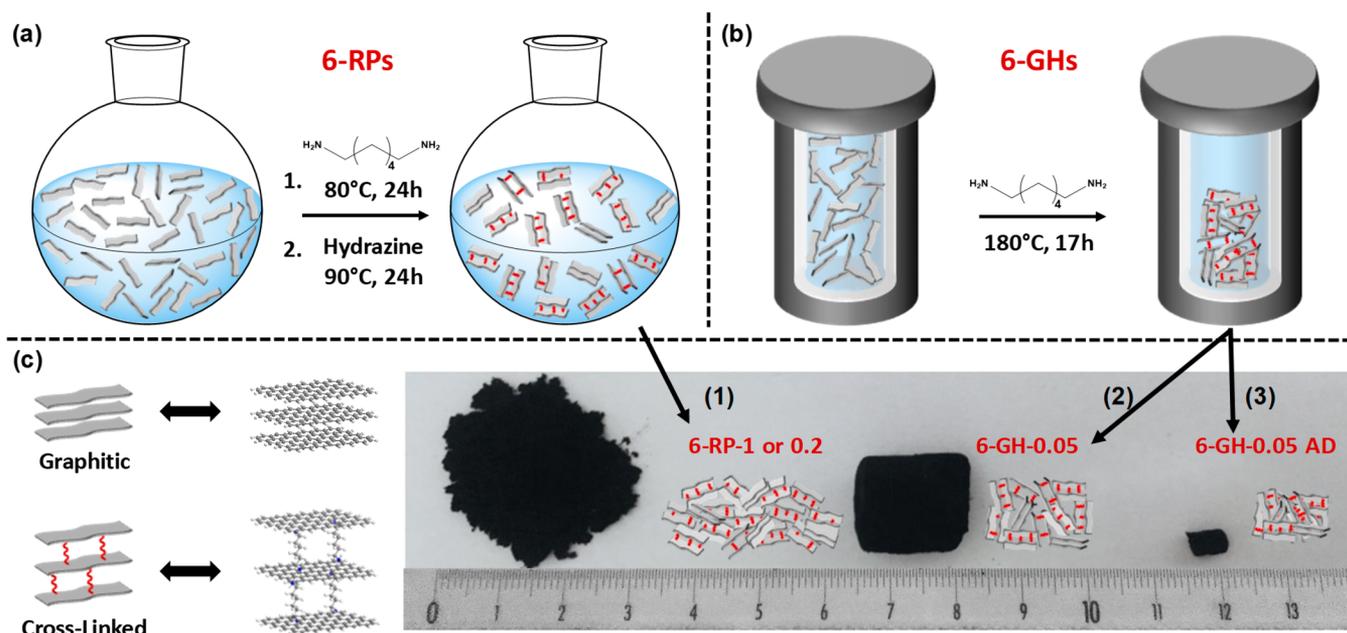
[a](a) 6 RPs are synthesized in two step process, cross linking and reduction, and (1) dried in vacuum oven at 100 °C for 24 h. (b) 6 GHs are synthesized in a one step process and either (2) freeze dried or (3) ambient dried (25 °C) for 2 days. (c) The graphitic and cross linked domains in each of the materials are represented schematically. The selected materials with chosen equivalents for the electrochemical analyses are presented here in the digital picture with a ruler for scale (cm).

desolvation and confinement of electrolytic ions in such pores restrict charge overscreening and result in efficient charge storage. Researchers have consequently explored matching pores sizes to electrolytic ions as an efficient strategy for improved energy storage.[17,18] However, difficulties in precisely tuning the pores in traditional carbons along with reliably determining pore sizes using gas sorption analyses have been major hindrances to swift progress.[2,8]

In parallel to ACs, various graphene derivatives have been proposed as potential materials for SCs owing to their high electrical conductivities, large surface areas, and mechanical flexibilities.[19] Reduced graphene oxide (RGO), readily prepared from graphene oxide (GO), is extensively studied as a model graphene like material.[20] RGO displays good power capability but suffers from low capacitances, as the reduced graphene sheets partially restack through $\pi-\pi$ interactions.[21] Various three dimensional (3D) architectures based on graphene (aerogels, films, and fibers) are being evaluated to mitigate such restacking with a focus on tuning the material porosity.[22] Exploring the layered structures of graphene derivatives for ion sorption could be another complementary approach to tuning the material porosity. The graphitic arrangement with 3.3 Å interlayer separation in restacked graphene derivatives is too small for ion sorption but could be tuned with an intercalant to exhibit an expanded layer structure.[23–26] It can be speculated that such expanded layered structures could offer additional ion sorption sites through ion desolvation and confinement effects as earlier seen with ultramicropores in CDCs.[11]

Recently, we synthesized a class of reduced pillared graphene materials (RPs) with varied interlayer separation using alkyl diamines as pillars and have investigated their use in SCs.[25] This comprehensive study using ions with various sizes showed that ions could access the interlayer graphene galleries as soon

as the naked ion sizes are smaller than the gallery height (defined by d spacing). Although this preliminary study has demonstrated ion sieving in pillared graphene materials, the observed capacitances remained only marginally better than RGO with appropriate electrolytic ions.[25] Further electro chemical impedance analyses have also shown extremely limited ion transport in these galleries.[27] These poor performances probably arose from excessive filling of the galleries with diamine pillars, leading to impeded ion transport to active sites.[28,29]

Herein, we report a substantial and simultaneous improve ment of both the power and energy densities in pillared materials following a two pronged strategy. First, the number of diamine pillars were systematically lowered for improved ion transport in the interlayer galleries of RPs. Second, a 3D macroporous graphene hydrogel was synthesized with this low density of pillars and with a different bulk porosity. Although pillared graphene materials with diamine cross linkers were proposed a decade ago, the nature of the cross linking is still debated.[23,24] Using one dimensional (1D) and two dimen sional (2D) solid state nuclear magnetic resonance (ssNMR) spectroscopy, we confirm the covalent attachment between diamines and graphene and notably demonstrate that the cross linking is similar for materials with different pillar densities and as well as for the graphene hydrogels. Electrochemical analysis using various electrolytic ions in SCs led to observation of ion sieving[30] in pillared graphene hydrogels. Ion sorption in the interlayer galleries of the pillared materials with tuned diamine pillar content enabled twice the capacitances (200 F·g^{-1}) compared to RGO (107 F·g^{-1}). Low densities of the gels were overcome by using an ambient drying approach, which led to high volumetric capacitance values of 210 F·cm^{-3}. The definitive evidence of covalent attachment of diamine pillars with control over pillar density combined with
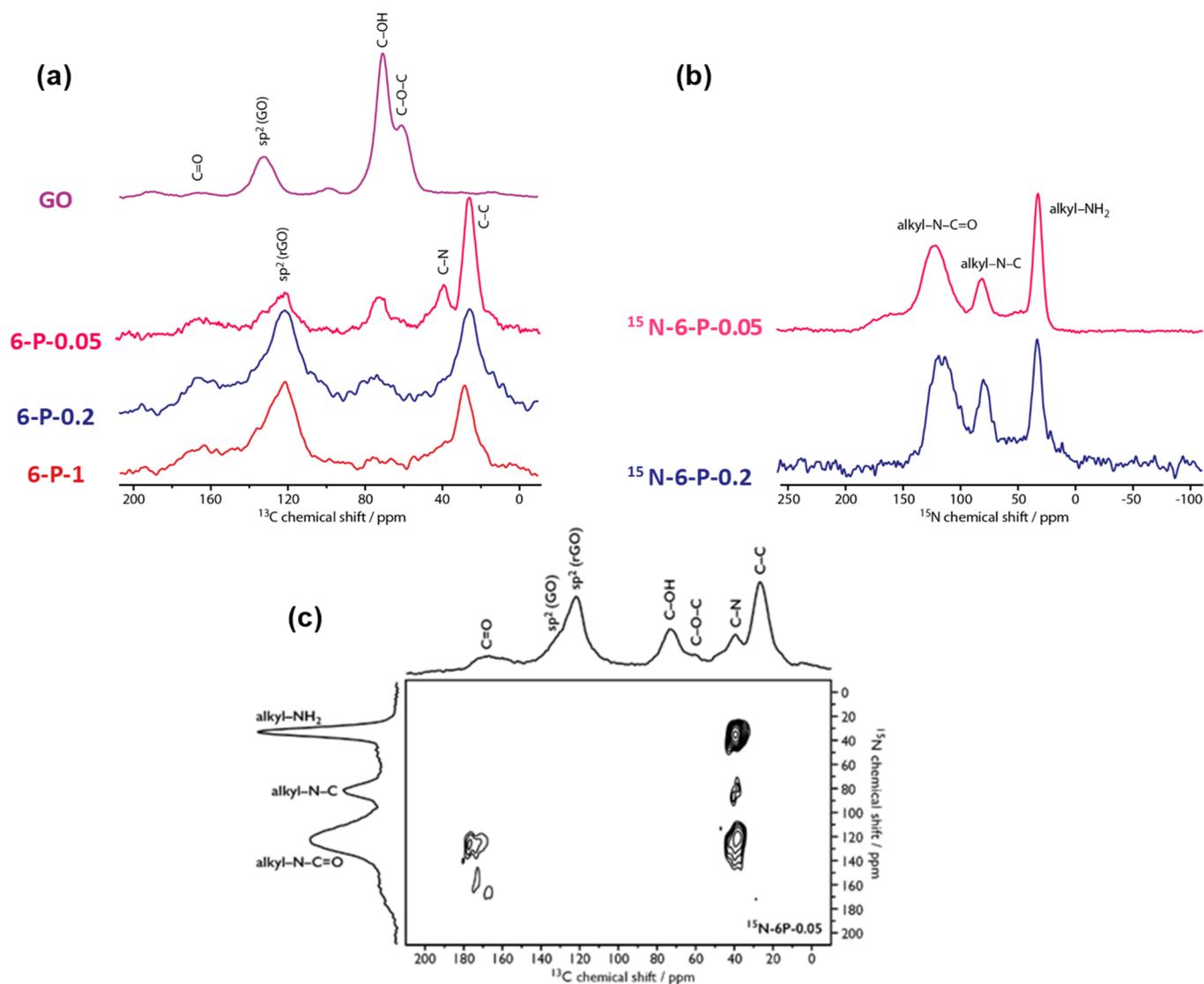
Figure 1. Solid state MAS NMR spectra recorded at 9.4 T (^{1}H Larmor frequency of 400 MHz) using a MAS frequency of 12 kHz. (a) {^{1}H}^{13}C cross polarization (CP) spectra (natural isotopic abundance) of graphene oxide (GO) and unreduced pillared materials (6 Ps) with varied diamine equivalents, recorded at 300 K. (b) {^{1}H}^{15}N CP spectra of unreduced pillared materials synthesized with different equivalents of ^{15}N labeled 1,6 diaminohexane, recorded at 300 K. (c) 2D ^{15}N−^{13}C TEDOR chemical shift correlation spectrum of 6 P 0.05 synthesized with ^{15}N labeled 1,6 diaminohexane, recorded at 100 K. Since the samples with varying numbers of equivalents were chemically reduced to different extents, consequently requiring different NMR acquisition times for a high signal to noise ratio, the spectra have therefore been scaled arbitrarily, and no relative quantitative information can be obtained.

their stability during long electrochemical tests (40,000 cycles) brings important perspectives to research on pillared materials for high performance SCs.

RESULTS AND DISCUSSION

GO has been extensively used as an ideal precursor for the synthesis of various graphene derivatives owing to its abundant oxygen functional groups.[31] The carboxylic groups at the edges and the epoxy groups distributed on the sheets offer substantial possibilities for functionalization with organic linkers.[32,33] Among others, alkyl diamines are efficient bifunctional groups that could react with these functionalities and cross link two GO sheets to form pillared graphene materials (Ps).[17,23] We chose 1,6 diaminohexane (6 diamine) as the pillar molecule due to the resulting *d* spacing (7.8 Å) and the ion sizes of tetraalkylammonium tetrafluoroborate (TAABF$_4$) salts (6.8− 9.5 Å for the cations and 4.8 Å for the anions).[25] After the

initial functionalization of GO with 6 diamine, the resulting 6 Ps were chemically reduced with hydrazine hydrate to give 6 RPs (Scheme 1a). Diamine functionalized graphene hydrogels (6 GHs) were synthesized in a one step hydrothermal process by reacting GO with 6 diamine (Scheme 1b).

Despite being synthesized in a one step process, the 6 GHs are sufficiently reduced during the hydrothermal process.[34] One equiv. of diamine to GO was chosen as an excess condition where the 2 Ns in diamine are available for 1 C in GO (see the Experimental Section for more details), and a series of 6 RPs and 6 GHs were synthesized using X equivalents of diamines with respect to GO and are named as 6 RP X or 6 GH X. "RGO" has also been synthesized as a control material by direct reduction of GO with hydrazine hydrate. The synthesized materials were characterized physico chemically using various spectroscopic techniques, and the porosity characteristics were analyzed using scanning electron
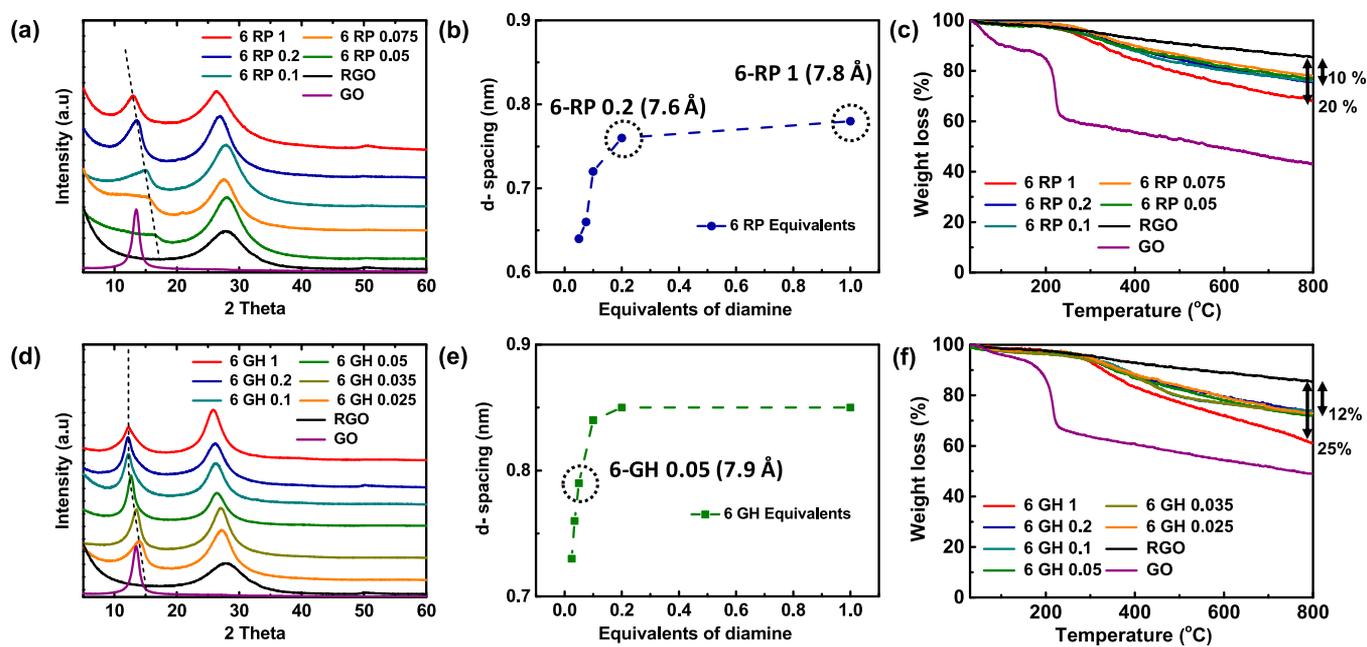
Figure 2. (a) XRD patterns of 6 RPs synthesized with various equivalents and (b) the corresponding *d* spacing values of the cross linked arrangement (CL) (peaks under dotted line). (c) TGA of various 6 RPs in the 30−800 °C temperature range at 5 °C·min^{-1} ramp rate. (d) XRD patterns, (e) *d* spacing values from CL peaks, and (f) TGA analyses of 6 GHs synthesized with varied equivalents of diamine. The specific 6 RPs and 6 GH chosen for electrochemical studies are highlighted with a dotted circle.

microscopy (SEM) and gas sorption studies. 1D and 2D magic angle spinning (MAS) ssNMR spectroscopy was performed using naturally abundant ^{13}C and ^{15}N labeled materials.

Pillared graphene materials were proposed in the early 2000s as interesting GO derivatives that could be readily prepared through reaction of the surface epoxy groups with nucleophilic primary amines.[26] Intercalation studies using diamines of various alkyl chain lengths have later allowed the tuning of the interlayer spacing of these graphene based materials.[23] However, the nature of the interaction (*i.e.* covalent and/or noncovalent) between alkyl diamines and GO sheets is not clearly understood. Fourier transform infrared (FTIR) analysis has mainly been used to study the presence of diamine in the pillared materials (Figure S1).[26] Indirect strategies such as swelling through solvent insertion,[24] sequential amine reactions,[23] and charge−discharge under polarization have been proposed to test the robustness of the pillared structures.[25] Although each of the indirect analyses supports the assumption of a covalent bond at each end of the diamine, a direct analysis of the interactions is still lacking. Direct observation and comparison of 6 RP with RGO through transmission electron microscopy (TEM) showed ordered graphene stacks in RGO, whereas the stacks in 6 RP appear rugose and non uniformly aligned, suggesting a chemical functionalization of the graphene sheets (Figure S2). Further atomic force microscopy (AFM) analyses showed elevated height profile in 6 RP compared to RGO, confirming the growth of particles in the *z* direction due to cross linking of graphene sheets by diamines (Figure S3). However, these microscopic observations along with the aforementioned indirect analyses do not provide direct evidence of the nature of interaction between diamines and graphene sheets. Hence, we obtained ^{13}C ssNMR spectra to detect the amine functionalization of GO, which was shown to occur *via* the epoxy groups,[35] and investigated ^{13}C and ^{15}N ssNMR spectra

to directly study the atomic environments of the graphene sheets and the nature of interaction with pillar molecules.

^{13}C ssNMR studies were conducted on GO and 6 Ps synthesized with different equivalents of diamines (0.05, 0.20, and 1.00), as shown in Figure 1. These experiments were restricted to 6 Ps rather than 6 RPs as the fully reduced samples display high electric conductivity, which prohibits magic angle sample spinning (MAS) ssNMR studies due to resulting problems in tuning the radio frequency circuit.[36] Moreover, as the 6 P samples are already partially reduced due to the mild reducing nature of the alkyl diamine, large degradation in NMR spectral quality is already observed for increasing numbers of equivalents. The ^{13}C NMR spectrum of the GO starting material shows the presence of C═O from carbonyls ($\delta(^{13}$C$) \sim 150-200$ ppm), aromatic carbons ($\delta(^{13}$C$) \sim 120-140$ ppm), C−OH from hydroxyls ($\delta(^{13}$C$) \sim 70$ ppm), and C−O−C from epoxides ($\delta(^{13}$C$) \sim 60$ ppm) (Figure 1a).[32,33,37] After reaction with 1,6 diaminohexane, the ^{13}C spectra of the 6 Ps are clearly different than that of GO. Additional ^{13}C signals arising from the alkyl chains of the diamine ($\delta(^{13}$C$) \sim 10-50$ ppm) and RGO ($\delta(^{13}$C$) \sim 120$ ppm) appear. Carbons in the alkyl chains in α position to the Ns of the diamines are also seen as a discrete ^{13}C peak ($\delta(^{13}$C$) \sim 40$ ppm) in 6 P 0.05. In 6 Ps, signals from the C−O−C epoxides and C−OH hydroxyls are drastically decreased relative to GO, and the signals from C═O moieties shift to amide positions ($\delta(^{13}$C$) \sim 150-180$ ppm). With a low number of diamine equivalents (6 P 0.05 and 6 P 0.2), some C−OH and C−O−C ($\delta (^{13}$C$) \sim 60-70$ ppm) functions remain, but the majority have been removed. These observations suggest covalent attachment of the amine groups in pillar molecules with epoxide and carboxylic groups on GO sheets. Still, it is noteworthy here that a simple reduction step and direct adsorption of the pillar molecule may also resemble the aforementioned spectral features.

The nature of the interaction between the pillar molecules and graphene was thus further investigated using ^{15}N labeled diamine as the pillar. The ^{15}N ssNMR spectra of [15]N 6 P 0.05 and [15]N 6 P 0.2 display three main peaks (Figure 1b): (i) $\delta(^{15}N) \sim 100-200$ ppm, assigned to N from amides (formed after reaction of diamine with carboxylic groups on GO sheets), (ii) $\delta(^{15}N) \sim 83$ ppm, which notably arises from N in α position relative to an aromatic carbon or a C−OH, and (iii) $\delta(^{15}N) \sim 34$ ppm, which is from unreacted amines. The signals at higher nitrogen chemical shifts ($\delta(^{15}N) > 50$ ppm) confirm that the pillar molecule is covalently grafted, while the peak from unreacted amine reveals that some remaining pillar molecules are either adsorbed on the graphene surface or are monografted. It is possible that the unreacted amine from monografted pillar molecules is able to form hydrogen bonds with functions on the opposite graphene layer, providing additional (noncovalent) interactions.

To gain further evidence on the location of the grafted pillar molecules, a through space (dipolar) 2D [15]N−[13]C correlation spectrum was recorded on [15]N 6 P 0.05. The z filtered transferred echo double resonance (TEDOR) experiment[38,39] was employed for this purpose, with short mixing time (1.3 ms) so as to detect only directly bonded [15]N−[13]C pairs.[39] The ^{13}C peak from the C−N carbons of the alkyl chain ($\delta(^{13}C) \sim 40$ ppm) correlates with the unreacted amine nitrogen signals ($\delta(^{15}N) \sim 34$ ppm), as one would expect for physisorbed or monografted alkyl diamines. Clear correlation peaks can be observed between amide nitrogen ($\delta(^{15}N) \sim 110-170$ ppm) and amide C=O ($\delta(^{13}C) \sim 165-180$ ppm) as well as between these same Ns and pillar C−N carbons ($\delta(^{13}C) \sim 40$ ppm) (Figure 1c). This proves that the diamines have reacted with the carboxyl functions on the GO sheets. Finally, the C−N pillar Cs ($\delta(^{13}C) \sim 40$ ppm) correlate with the −C−N−C−Ns in α position to aromatics or hydroxyls ($\delta(^{15}N) \sim 83$ ppm), indicating that the diamine has been grafted to the graphene surface through reactions with epoxides. Overall, these 2D ssNMR experiments on the pillared graphene materials confirm the covalent grafting of alkyl diamines to the basal planes and edges of graphene sheets. Note that 6 GH 0.05 was also examined with ssNMR, and it exhibits the same ^{13}C and ^{15}N spectral features as 6 P 0.05 (Figure S4).

X ray diffraction (XRD) patterns were obtained to directly analyze the layered structures in the synthesized materials (Figure 2a,d). Freeze dried GO shows a sharp peak at a 2θ of 13.5°, which relates to a d spacing of 7.6 Å, indicating a high degree of oxidation of the oxidized graphite precursor. Upon direct reduction of GO with hydrazine hydrate, the resulting RGO displays a broad peak at 28° corresponding to a graphite like pattern (G), suggesting removal of oxygen groups and partial restacking of the reduced graphene sheets.[40] Diamine functionalization of GO in 6 RPs and 6 GHs results in two distinct diffraction peaks around 25−27° and 11−13°. The peaks at higher angles correspond to G stacking and indicate a reduction degree close to that of RGO. The peaks below 20°, corresponding to diamine intercalation and cross linking (CL) of the graphene sheets, shift with respect to the number of equivalents used.[25] With increasing number of equivalents, the CL peaks of both 6 RPs and 6 GHs systematically shift towards lower angles (higher d spacing values). The obtained d spacing values for 6 RP (Figure 2b) and 6 GH (Figure 2e) initially increase and then saturate at 0.2 and 1 equiv. for 6 RP and 6 GH, respectively. The observed d spacing values fit well into a chemisorption type model and suggest a grafting of the

alkyl diamines on the graphene surfaces instead of a simple physisorption (Figure S5), in line with the NMR data.

A closer look at the shape and position of the CL peak reveals important information about the evolution of 6 RP and 6 GH structures with different number of equivalents. 6 RP shows relatively sharper peaks with 1 and 0.2 equiv., whereas increasingly broad and less intense peaks are seen with lower equivalents. On the other hand, whatever the number of equivalents, 6 GHs exhibit similar CL peak intensities and width. Nevertheless, in both materials, lower equivalents of diamine lead to a lower average d spacing, probably due to reduced availability of diamines to react with all epoxides (*vide supra*). 6 RP saturates at a lower d spacing of ∼7.8 Å, whereas 6 GH saturates at 8.5 Å (*cf.* Figure 2b,e). Moreover, 6 GH saturates faster, at 0.1−0.2 equiv., suggesting a relatively higher density of grafted diamines. This evolution of shapes and the higher d spacing values in 6 GH could probably be related to the stronger reaction conditions used to prepare GHs compared to RPs. A comparison of the ^{13}C ssNMR spectra of 6 P 0.05 and 6 GH 0.05 (Figure S4a) shows that 6 GH 0.05 consumes nearly all of the epoxides from the GO precursor, whereas 6 P 0.05 still has a considerable number of unreacted epoxides. Moreover, the ^{15}N spectra show a relatively narrow peak for unreacted amine in 6 P 0.05 and a relatively less intense and broader corresponding peak in 6 GH 0.05 (Figure S4b), suggesting that more amines have reacted in the 6 GHs and also that those that remain unreacted in the 6 GHs are blocked in various environments, probably through hydrogen bonds with the opposite graphene layer. The stronger reaction conditions used to prepare 6 GHs thus lead to enhanced cross linking with diamines and result in higher d spacing values for same number of equivalents compared to 6 RPs. These reaction conditions enable the vast majority of diamines anchored on one GO sheet to find a functional group on another GO sheet, growing larger cross linked particles, which can explain the sharper CL peaks observed for 6 GHs.

The thermal degradation responses of the materials under N_2 are shown in Figure 2c,f. GO displays two distinct weight loss events corresponding to the removal of adsorbed water below 100 °C and the decomposition of surface oxygen functional groups around 200 °C. A steady drop beyond 200 °C is generally attributed to gradual removal of stable functionalities.[41] RGO shows only a slight weight loss throughout the temperature range, suggesting an effective removal of oxygen groups in its synthesis. Both 6 RPs and 6 GHs show a broad weight loss between 300 and 500 °C and a gradual weight loss similar to RGO. This broad weight loss beyond the boiling point of 6 diamine (204 °C) is attributed to the removal of nonlabile 6 diamine species.[25] Moreover, the absence of loss due to moisture or oxygen functionalities further confirms the reduced nature of the functionalized materials. In addition, the weight losses between different 6 RPs or 6 GHs are smaller for lower equivalents, signaling a reduction in diamine grafting densities. Taking RGO as the reference, 6 RP displays weight losses of 20 and 10% with 1 and 0.2 equiv., respectively, whereas 6 GH exhibits 25 and 12% (for the same number of equivalents).

In summary, GHs and RPs are both cross linked with alkyl diamines, are reduced, and are chemically similar despite synthesis under different reaction conditions. To study the impact of the number of diamine pillars in the galleries and the bulk porosities on the overall ion sorption in SCs, we chose 6 RP 1 as the sample with the highest number of diamine pillars
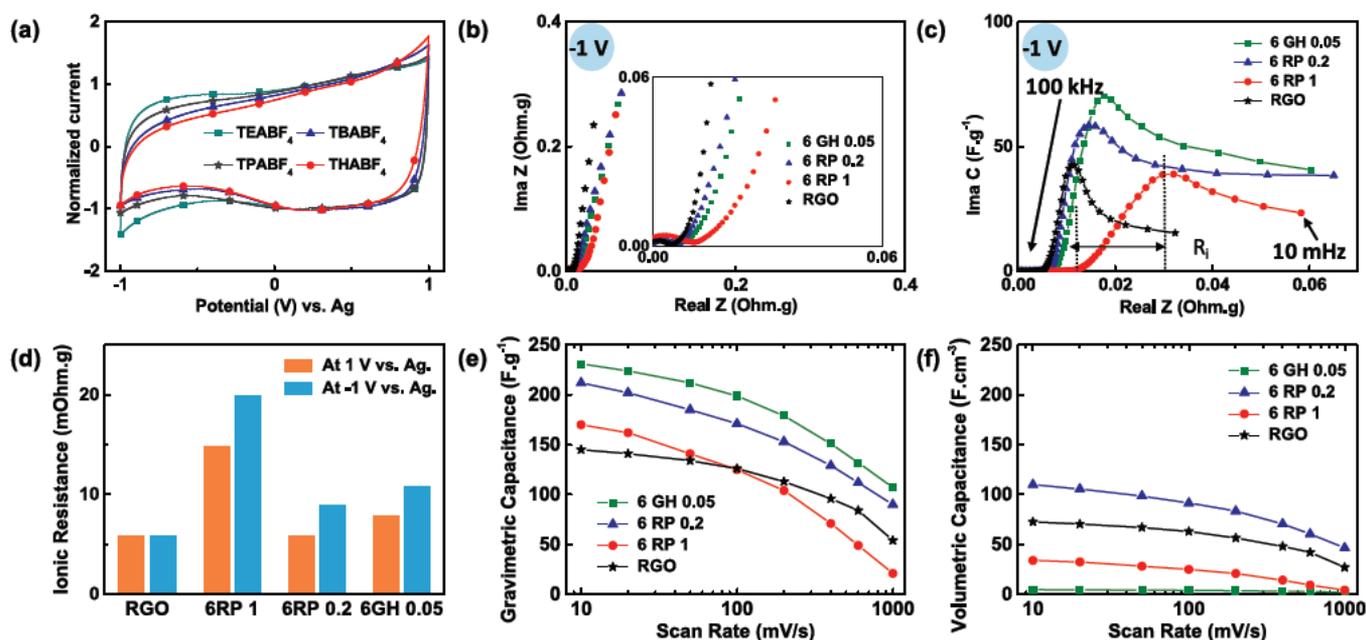
Figure 3. (a) Normalized three electrode CVs of 6 GH 0.05 obtained at a scan rate of 0.02 V·s^{-1} in the voltage range of −1 to 1 V *vs* Ag in 1 M solutions of TAABF$_4$ salts in acetonitrile (AN). Electrochemical impedance measurements and CVs were performed on all the synthesized materials in a three electrode configuration using 1 M TEABF$_4$/AN as electrolyte. (b) Normalized Nyquist plots obtained at −1 V *vs* Ag. A zoom of the high and midfrequency regions is shown in the inset. (c) Imaginary capacitance vs real impedance plots at −1 V *vs* Ag. The double arrow indicates the ionic resistance (R_i) in 6 RP 1. (d) R_i values obtained for the synthesized materials at 1 V and −1 V *vs* Ag. (e) Gravimetric and (f) volumetric specific capacitances of the synthesized materials obtained from three electrode CVs performed at 0.01−1 V·s^{-1} scan rates in a larger electrochemical window of −1.3 to 1.5 V *vs* Ag.

and 6 RP 0.2 and 6 GH 0.05 as samples with similar *d* spacing to 6 RP 1 (~7.8 Å) but with lower diamine filling contents (Table S1). RGO, with no CL galleries, acts as a control sample. The porosity and morphologies of these chosen materials were analyzed by N$_2$ gas sorption[42] and SEM. The tested materials exhibit type II adsorption−desorption isotherms with a hysteresis loop, indicating the presence of both micro and mesopores (Figure S6a).[43] RGO has the highest specific surface area (SSA) of 330 m^2·g^{-1}, whereas 6 RP 1, 0.2 and 6 GH 0.05 display lower SSA values of 140, 200, and 200 m^2·g^{-1}, respectively (Table S1). Previous reports on pillared materials have suggested that the pillars inside the interlayer galleries could sterically hinder gas sorption and render the galleries as closed pores.[29] This could be a plausible explanation for the lower SSA values of the 6 RPs and 6 GH 0.05 compared to RGO. Indeed, if the gas molecules were probing the galleries, one would expect significant adsorption at low relative pressures. Additionally, changing the pillar density from 1 to 0.05 equiv. would have also shown changes in the adsorption at low relative pressures. These observations provide a strong reason to believe that the gas sorption experiments do not analyze the galleries. Nevertheless, despite such observation, the applied potential on the electrode during electrochemical processes has been reported to provide additional driving force for ion sorption in such galleries.[25] The calculated pore size distributions show a major presence of micropores in RGO and mesopores in 6 RPs and 6 GH 0.05, respectively (Figure S6b). The expected 3D macroporous network in 6 GH 0.05 might be too big to be probed through gas sorption analysis.[22] The comparison of SEM images of 6 RP 0.2 (Figure S7c) and 6 GH 0.05 (Figure S7d) shows a 3D network of large macropores arising from the hydrothermal treatment. Further, it was, thus, interesting to investigate the

electrochemical performances of these contrasting pillared materials displaying similar *d* spacing but varying in diamine content and macroporosity; 6 RP 1 (high diamine content), 6 RP 0.2 (low diamine content), and 6 GH 0.05 (low diamine content and different macroporosity).

ELECTROCHEMICAL ANALYSES

Ion Sieving. Cyclic voltammetry (CV) and electrochemical impedance spectroscopy (EIS) studies were performed in SC lab cells to analyze 6 RP 1, 6 RP 0.2, 6 GH 0.05, and RGO. Although the synthesized 6 RP 0.2 and 6 GH 0.05 have similar *d* spacing to 6 RP 1 (~ 7.8 Å), the two materials were first analyzed in three electrode configuration to probe their ion sieving capabilities. Various 1 M TAABF$_4$ salts in acetonitrile (AN) with increasing cation size and a constant anion size were used as electrolytes: ethyl (TEA$^+$) 6.8 Å, propyl (TPA$^+$) 7.6 Å, butyl (TBA$^+$) 8.2 Å, and hexyl (THA$^+$) 9.5 Å, with BF$_4^-$ 4.8 Å.[44,45] Earlier ion sieving investigations under positive and negative polarization from open circuit potentials (OCV) of ~0.1 V *vs* Ag have enabled analyses of anion and cation sorption in SCs.[46] 6 RP 1 displays rectangular capacitive curves with smaller ions but distorted curves and reduced currents under negative polarization when the ion sizes are close to, or higher than, the *d* spacing (Figure S8b). Similar tests with 6 RP 0.2 and 6 GH 0.05 show quasi ideal capacitive behavior under positive polarization where the anion is smaller than the *d* spacing in the materials (Figure 3a and Figure S8c). Under negative polarization, both materials show gradual reduction in currents as the cation sizes approach the *d* spacing in the materials. Since 6 RP 0.2 and 6 GH 0.05 both show a lack of ultramicro interparticle pores, the observed sieving can be attributed to the interlayer galleries. Overall, these results affirm ion access to the interlayer galleries in 6 RP 0.2 and 6

Scheme 2. Schematic Representation of the Ion Transport in the Synthesized Materials[a]

External graphene surfaces
(RGO)

Densely filled galleries

Sparsely filled galleries
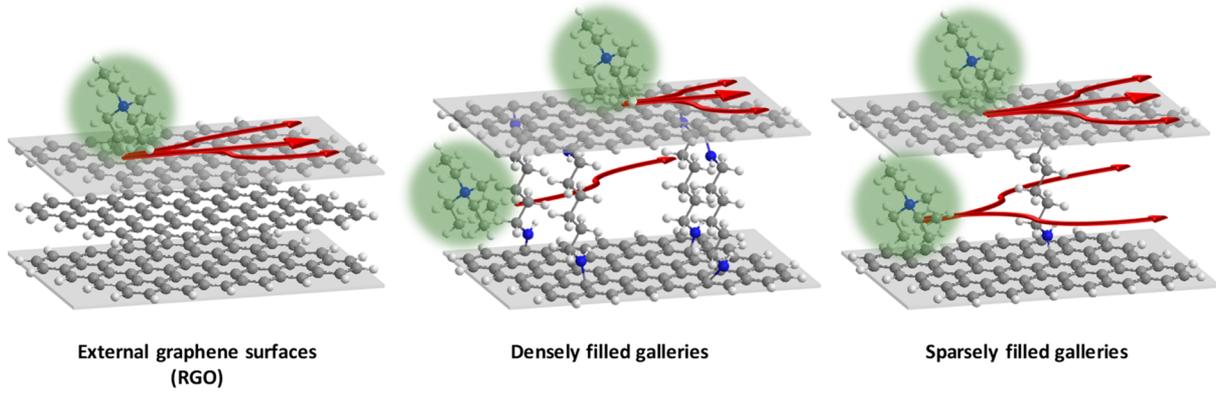
[a]Ion sorption in RGO occurs on the graphene surfaces in micro/mesopores and the ion transport is relatively easy. In pillared materials, in addition to the external graphene surfaces, ion sorption occurs in the inter layer galleries. The diamine filling density in the galleries regulates the ion transport in these materials.

GH 0.05 and highlight them as suitable materials to study the ion transport in between graphene layers.

Impedance Analyses. The ion transport dynamics in the synthesized materials were studied using EIS measurements. OneM TEABF$_4$/AN was chosen as the electrolyte due to its sufficiently small ion sizes that could access the interlayer galleries of the pillared materials. Impedance responses were recorded at 1 V and −1 V vs Ag to obtain the distinct anion and cation transport characteristics, respectively, and the normalized complex plane Nyquist plots are displayed in Figure 3b and Figure S9a. These plots can be divided into three regions of high, medium, and low frequencies.[47,48] At high frequencies, only the electrical conductivity of the electrode together with bulk electrolyte ionic conductivity can be seen; thus, SC electrodes behave like a resistor ($Z'' = 0$). At low frequencies, a sharp increase of the imaginary part of the impedance ($-Z''$), related to capacitive behavior, is seen. The intermediate 45° region is associated with the electrolyte resistance arising from ion transport in the porous network of the electrode. At 1 V vs Ag, the pillared materials and RGO display similar capacitive like Nyquist curves and indicate comparable anion transport behavior (Figure S9a). A closer look at the high frequency region (inset) shows a slightly longer 45° region for 6 RP 1 compared to others. The slight differences of ion transport are more obvious under −1 V vs Ag when the larger TEA$^+$ cations are involved. At −1 V vs Ag, 6 RP 1 exhibits a large 45° region in the medium frequency range compared to the others (Figure 3b), signaling higher ion transport resistance. 6 RP 0.2 and 6 GH 0.05, which possess a low number of diamine pillars, show significantly improved ion transport with a smaller 45° region than 6 RP 1. This difference in ion transport highlights the merits of having fewer pillars. Interestingly, 6 RP 0.2 and 6 GH 0.05 seem to show similar curves despite their differences in material macroporosity.

The obtained Nyquist plots give an idea about the relative impedances of the materials but are difficult to use to extract information about frequencies. The Complex Capacitance model, reported by Taberna $et\ al.$[49] and derived from Cole and Cole,[50] provides an easier way of studying frequency responses of the materials. The real and imaginary parts of the capacitance, defined as $C'(w)$ and $C''(w)$ in eqs 1 and 2, respectively, represent the available stored energy with respect to frequency and energy losses during the charge storage, respectively. $Z'(w)$ and $Z''(w)$ are the real and imaginary parts of impedance $Z(w)$, where w is the frequency.

$$C'(w) = \frac{-Z''(w)}{w\,|Z(w)|^2} \quad (1)$$

$$C''(w) = \frac{-Z'(w)}{w\,|Z(w)|^2} \quad (2)$$

As C'' represents the irreversible losses in a SC, we studied $C''(w)$ with respect to $Z'(w)$ (Figure 3c and Figure S6b). Such an analysis relates energy losses to the impedance in various frequency regions and also enables an easier determination of the distinct ionic resistances (R_i) in the materials.[25,27] The $C''(w)$ vs $Z'(w)$ plots at 1 V vs Ag show clear differences between 6 RP 1 and the other materials (see Figure 3c and Figure S9b). 6 RP 1 displays a broader curve and a maximum imaginary capacitance that occurs at higher resistances compared to RGO, 6 RP 0.2, and 6 GH 0.05. With the larger TEA$^+$ cation at −1 V vs Ag, the maximum imaginary capacitance of 6 RP 1 shifts to even higher resistances (see Figure 3c). The R_i values at both potentials were readily obtained from the $C''(w)$ vs $Z'(w)$ curves and are shown in Figure 3d. R_i values for 6 RP 0.2 and 6 GH 0.05 are between 6 and 12 mΩ·g under 1 V and −1 V, whereas 6 RP 1 displays higher R_i values of 15 and 20 mΩ·g, respectively. These quantified ionic resistances highlight the impact of the number of pillars on the ion transport inside the galleries. Importantly, R_i values obtained for the pillared materials with lower numbers of equivalents (6 RP 0.2 and 6 GH 0.05) are closer to that of RGO, which has no cross linked galleries. This demonstrates the significance in optimizing these pillared materials.

The imaginary $C''(w)$ vs w curves have a maximum at a frequency f_0 that defines the transition between purely resistive and capacitive behaviors of a SC (see Figure S10a,b). This frequency, known as the knee frequency, defines the time constant (τ_0) as the minimum time required to extract half of the capacitance from a SC.[49] The τ_0 values of a SC depend on the combination of all the ionic, electrical, and cell resistances. 6 RP 0.2 and 6 GH 0.05 exhibit τ_0 values of 5 and 7 s, respectively, under both polarizations and are close to that of RGO (5 s). 6 RP 1 shows high values of 13 and 17 s under
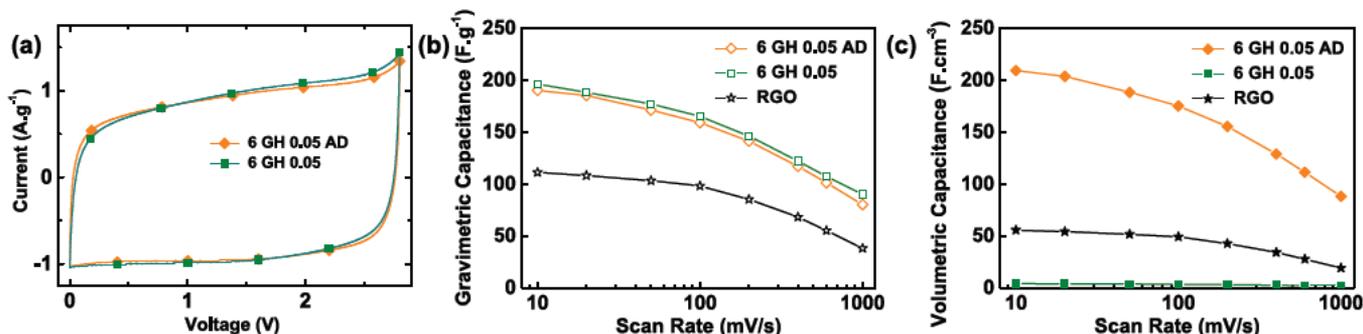
Figure 4. (a) CVs of freeze dried 6 GH 0.05 and ambient dried 6 GH 0.05 AD at 0.02 V·s^{-1} scan rate in 1 M TEABF$_4$/AN. (b) Gravimetric and (c) volumetric specific capacitances of the materials obtained from two electrode CVs in 1 M TEABF$_4$/AN, performed at 0.01−1 V·s^{-1} scan rates.

negative and positive polarization, respectively (see Table S2). These low τ_0 values for 6 RP 0.2 and 6 GH 0.05 are highly linked to the improved ion transport dynamics, thanks to the lower the number of pillars in the galleries, and indicate better power capabilities in SCs. The real $C'(w)$ vs w curves provide an estimation of the available energy stored in the synthesized materials (Figure S10c,d). The maximal $C'(w)$ values for 6 RP 0.2 and 6 GH 0.05 under both polarizations are nearly two times larger than that of 6 RP 1. The low number of pillars probably gives access to additional active sites inside the interlayer galleries that were previously inaccessible, leading to higher capacitances. Notably, the $C'(w)$ values of 6 RP 0.2 and 6 GH 0.05 are also twice that of RGO. Since RGO does not have any cross linked galleries, this difference could be attributed to an increased number of adsorption sites inside the cross linked galleries of 6 RP 0.2 and 6 GH 0.05.

This EIS analysis clearly indicates the role of pillars in the ion transport dynamics in these materials. Based on the understanding provided above, Scheme 2 illustrates the improved ion transport and ion sorption capabilities in the pillared materials with fewer pillars. The τ_0 and R_i values of the optimized 6 RP 0.2 and 6 GH 0.05 account for the improved ion transport compared to 6 RP 1 and are similar to that of RGO. This highlights the importance of fine tuning the number of pillars in the material to efficiently control the ion transport as well as to increase accessibility to adsorption sites. Indeed, ion sorption in RGO occurs on the external graphene surfaces, and not between the sheets (Scheme 2, left), whereas the pillared materials allow for additional sorption sites inside the cross linked galleries (Scheme 2, middle and right), leading to the higher capacitances observed for the latter.

Another interesting aspect of ion transport that was expected to be elucidated from the EIS studies was the role of additional macroporosity in 6 GH 0.05 compared to 6 RP 0.2. Instead of an improved ion transport that one could expect from the 3D percolating network in 6 GH 0.05, slightly better τ_0 and R_i values were actually observed for 6 RP 0.2. We believe that the two different synthesis procedures for GHs and RPs are responsible for this. As inferred from the thermal gravimetric analyses (TGA) and XRD data (vide supra), these two synthesis protocols lead to different relative pillar densities and also can account for different electrical conductivities observed for 6 RP 0.2 (180 S/m) compared to 6 GH 0.05 (100 S/m).

Power Capability and Volumetric Performances. The observed enhanced ion transport characteristics were further investigated through a power capability study. Three electrode

CVs were performed in a larger electrochemical window of −1.3 to 1.5 V vs Ag (a voltage window of 2.8 V) at scan rates of 0.01−1 V·s^{-1} (Figure 3e,f) in TEABF$_4$/AN. RGO exhibits 145 F·g^{-1} at 0.01 V·s^{-1} and decreases to 50 F·g^{-1} at 1 V·s^{-1}, whereas 6 RP 1 exhibits slightly higher values of 170 F·g^{-1} at 0.01 V·s^{-1} but shows a poorer performance of 20 F·g^{-1} at 1 V·s^{-1}. The observed values for RGO and 6 RP 1 are slightly higher than those reported earlier using a 2 V window.[25] This increase is probably due to electrowetting of the electrodes in the larger 2.8 V window.[51] Upon reducing the number of pillars, 6 RP and 6 GH both show much improved capacitances (205 F·g^{-1} for 6 RP 0.2 and 230 F·g^{-1} for 6 GH 0.05 at 0.01 V·s^{-1}) and power capabilities (90 F·g^{-1} for 6 RP 0.2 and 107 F·g^{-1} for 6 GH 0.05 at 1 V·s^{-1}). As previously discussed, this increase in capacitance when lowering the pillar number is due to the enhanced ion access and transport to the active sites inside the interlayer galleries. Furthermore, fewer pillars also reduce the relative weight of the electrochemically inactive diamine, aiding the overall specific capacitances. Together, this increased accessibility to active sites and reduced hindrance to ion motion result in materials (6 RP 0.2 and 6 GH 0.05) with twice the power capabilities of RGO. A comparison of 6 RP 0.2 and 6 GH 0.05 shows different capacitances but similar power capabilities. While the relative ion transport kinetics have been evoked above, the higher capacitance of 6 GH 0.05 compared to that of 6 RP 0.2 could be attributed to a higher accessibility brought about by the 3D percolating network in 6 GH 0.05. Overall, the high specific capacitances of all the pillared materials (with SSA <200 m^2/g) compared to RGO (with SSA less than 330 m^2/g) confirms that the surface area accessible to ion sorption and gas sorption is different.

The synthesized pillar materials offer increased gravimetric capacitances compared to RGO, but they have low volumetric capacitances owing to their low material densities. RGO, 6 RP 0.2, and 6 GH 0.05 exhibit 70, 110, and 4 F·cm^{-3} with their material densities of 0.5, 0.25, and 0.02 g.cm^{-3}, respectively (see Figure 3f). However, the graphene hydrogel (6 GH 0.05) provides an opportunity to enhance the material density through a simple ambient drying technique (Scheme 1). A slow evaporation of the water in the hydrogel is reported to shrink the large macro pores and densify the hydrogel.[52] Hence, we synthesized 6 GH 0.05 AD (ambient dried) as a high density counterpart to 6 GH 0.05; the material density increased from 0.02 to 1.1 g.cm^{-3}. The XRD pattern of 6 GH 0.05 AD still shows a CL peak corresponding to the expected interlayer spacing of 7.8 Å (see Figure S11a), and the SEM

images indicate clear shrinking and densification upon ambient drying (see Figure S12).

Two electrode symmetrical cells of 6 GH 0.05 and 6 GH 0.05 AD were fabricated and studied in a 2.8 V window. The CVs obtained at 0.02 V·s^{-1} in TEABF$_4$/AN show rectangular shaped curves with similar current densities for both 6 GH 0.05 and 6 GH 0.05 AD (see Figure 4a). The gravimetric power capabilities of the materials from 0.01 to 1 V·s^{-1} show identical profiles for both materials (see Figure 4b). The close performances of the freeze dried and ambient dried pillared materials suggest that the shrinking of the macroporous network in 6 GH 0.05 AD results in negligible loss to the overall ion sorption and ion transport characteristics. Further EIS analyses of both the samples under a negative polarization of −1 V vs Ag have confirmed their similar ion transport characteristics. Nyquist plots and additional analyses (Ima C vs Real Z and Bode diagrams) from the frequency responses of both the materials appear identical (Figure S13) and close τ_0 values of 7.1 and 7.1 s and R_i values of 13 and 15 mΩ·g for 6 GH 0.05 and 6 GH 0.05 AD, respectively, were noted. These observed similarities in ion transport characteristics despite densification could be attributed to the ambient drying process which shrinks large macropores into mesopores that are large enough to support facile ion transport.

Upon ambient air drying, the volumetric capacitance of 6 GH 0.05 AD has dramatically increased with respect to that of 6 GH 0.05: from 4 to 200 F·cm^{-3}. Notably, this value is four times higher than that of RGO, calculated to be around 50 F·cm^{-3} (see Figure 4c). Cycling of 6 GH 0.05 AD at a high scan rate of 1 V·s^{-1} for 40,000 cycles resulted in 93% capacitance retention with nearly 100% columbic efficiency (Figure S14). Additionally, various spectroscopic (XPS, IR, NMR) and electrochemical analyses performed on the cycled electrodes have confirmed the robustness of the pillared structure during electrochemical cycling (Figures S15 and S16). The observed volumetric values are among the best for carbon based SCs with double layer charge storage (see Table S4 for a comparison).[53] The straightforward single step synthesis of 6 GH and the subsequent ambient drying process add further merit to the current approach compared to others. Additionally, the proposed pillared materials also provide avenues toward even higher performances. Improving the type of pillar (e.g. electrochemically active), the relative content of cross linked particles compared to graphitic like arrangements, and/or trapping redox molecules in the galleries could be a few such strategies. In addition to the field of energy storage, the pillared graphene architectures offer great scope for applications in other scientific fields such as gas storage, water desalination, and membrane filtration.

CONCLUSIONS

Pillared graphene materials were synthesized to mitigate the graphitic restacking in graphene based materials by separating graphene sheets with a pillar molecule, providing additional ion sorption sites for SCs. The physicochemical characterization of the materials demonstrated that the pillar molecule acts as a spacer, forming cross linked graphene galleries. In particular, ssNMR studies confirmed the covalent nature of the interaction between the pillars and graphene sheets. Thus, the synthesized graphene galleries are structurally robust for long cycle life in SCs. The electrochemical performances of the synthesized materials in SCs were compared to RGO, which has no pillared structures. Pillared graphene materials synthesized with an optimized number of pillars exhibit high specific capacitances of 185 F·g^{-1} (vs 107 F·g^{-1} for RGO), confirming the enhanced electrochemically active surface area. The number of pillars in the galleries was found to have a significant influence on the SC performances; a dense filling of the galleries led to lower capacitances and poor power capability, whereas sparse filling improved both. These results show that the optimized number of pillars preserves gallery structures, provides ion access to new active sites, and offers efficient ion transport pathways. Finally, pillared graphene hydrogels, synthesized to contain additional 3D interconnected porous networks, delivered even higher capacitances of 200 F·g^{-1} and, once air dried, volumetric capacitances of 210 F·cm^{-3}. Overall, covalent and sparsely pillared structures add encouraging perspectives toward achieving high performance graphene based SCs.

EXPERIMENTAL SECTION

Reduced Pillared Graphene Material (6-RPs). An aqueous solution of well dispersed 5 mg·mL^{-1} GO was prepared and used as a precursor for all syntheses (details in Supporting Information).[54] 6 RPs were synthesized in a two step process of cross linking with 1,6 diaminohexane and further chemical reduction with hydrazine hydrate. One molar equivalents of diamine to GO was used as a sufficiently excess condition providing 2 molar equivalents of N for 1 C in GO. The formula weight of the synthesized GO was calculated as 13.01 g from the elemental composition obtained by XPS. Materials with 1, 0.2, 0.1, 0.075, and 0.05 equiv of diamine were synthesized using 75 mL of GO (28 mmol) and 3.27, 0.651, 0.325, 0.243, and 0.162 g of 1,6 diaminohexane, respectively. 75 mL of GO and diamine dissolved in 75 mL of ethanol was sonicated for 10 min and then heated under reflux at 80 °C for 24 h while being continuously stirred. The reaction mixtures were later cooled, filtered through P3 filter, and washed with copious amounts of ethanol, water, and ethanol again, sequentially. The obtained product was then dried in the vacuum oven at 100 °C overnight. The obtained pillared materials were further reduced by treating with excess hydrazine hydrate at 90 °C for 24 h while being continuously stirred. The obtained reduced pillared materials were cleaned with an excess of water, dried under a vacuum at 100 °C, and labeled as the respective 6 RPs.

Pillared Graphene Hydrogels (6-GHs). An aqueous solution of well dispersed 5 mg·mL^{-1} GO was prepared and used as a precursor for all syntheses. 6 GHs were synthesized in a one step hydrothermal process using 1,6 diaminohexane as cross linking agent. Each synthesis was performed with 15 mL of GO (5.6 mmol) with 1, 0.2, 0.1, 0.05, 0.035, and 0.025 equiv of diamine using 1.21, 0.242, 0.121, 0.060, 0.042, and 0.016 g of 1,6 diaminohexane, respectively. Fifteen mL of GO and the required amount of diamine were sonicated for 10 min and then reacted in a sealed 23 mL vessel at 180 °C for 17 h. The resulting hydrogel was cleaned with excess ethanol and water sequentially and freeze dried using liquid N$_2$ to obtain 6 GH aerogels. Ambient dried gels were obtained by drying the hydrogels at room temperature for 2 days, and the remaining moisture was removed by heating in vacuum at 80 °C overnight.

ASSOCIATED CONTENT

● **Supporting Information**

AUTHOR INFORMATION

Corresponding Author
*E mail: florence.duclairoir@cea.fr.

ORCID

Patrice Simon: 0000 0002 0461 8268
Gaël De Paëpe: 0000 0001 9701 3593
Florence Duclairoir: 0000 0003 0257 0501

Notes

The authors declare no competing financial interest.

REFERENCES

(1) Conway, B. E. *Electrochemical Supercapacitors Scientific Fundamentals and Technological Applications*; Springer International Publishing: NewYork, 1999.

(2) Salanne, M.; Rotenberg, B.; Naoi, K.; Kaneko, K.; Taberna, P. L.; Grey, C. P.; Dunn, B.; Simon, P. Efficient Storage Mechanisms for Building Better Supercapacitors. *Nat. Energy* 2016, 1, 16070.

(3) Simon, P.; Gogotsi, Y. Materials for Electrochemical Capacitors. *Nat. Mater.* 2008, 7, 845−854.

(4) Zhang, L. L.; Zhao, X. S. Carbon Based Materials as Supercapacitor Electrodes. *Chem. Soc. Rev.* 2009, 38, 2520−2531.

(5) Chmiola, J.; Yushin, G.; Gogotsi, Y.; Portet, C.; Simon, P.; Taberna, P. L. Anomalous Increase in Carbon Capacitance at Pore Sizes Less Than 1 Nanometer. *Science* 2006, 313, 1760−1763.

(6) Vix Guterl, C.; Frackowiak, E.; Jurewicz, K.; Friebe, M.; Parmentier, J.; Béguin, F. Electrochemical Energy Storage in Ordered Porous Carbon Materials. *Carbon* 2005, 43, 1293−1302.

(7) Raymundo Piñero, E.; Kierzek, K.; Machnikowski, J.; Béguin, F. Relationship between the Nanoporous Texture of Activated Carbons and Their Capacitance Properties in Different Electrolytes. *Carbon* 2006, 44, 2498−2507.

(8) Béguin, F.; Presser, V.; Balducci, A.; Frackowiak, E. Carbons and Electrolytes for Advanced Supercapacitors. *Adv. Mater.* 2014, 26, 2219−2251.

(9) Chmiola, J.; Largeot, C.; Taberna, P. L.; Simon, P.; Gogotsi, Y. Desolvation of Ions in Subnanometer Pores and Its Effect on Capacitance and Double Layer Theory. *Angew. Chem., Int. Ed.* 2008, 47, 3392−3395.

(10) Largeot, C.; Portet, C.; Chmiola, J.; Taberna, P. L.; Gogotsi, Y.; Simon, P. Relation between the Ion Size and Pore Size for an Electric Double Layer Capacitor. *J. Am. Chem. Soc.* 2008, 130, 2730−2731.

(11) Merlet, C.; Péan, C.; Rotenberg, B.; Madden, P. A.; Daffos, B.; Taberna, P. L.; Simon, P.; Salanne, M. Highly Confined Ions Store Charge More Efficiently in Supercapacitors. *Nat. Commun.* 2013, 4, 2701.

(12) Tsai, W. Y.; Taberna, P. L.; Simon, P. Electrochemical Quartz Crystal Microbalance (EQCM) Study of Ion Dynamics in Nano porous Carbons. *J. Am. Chem. Soc.* 2014, 136, 8722−8728.

(13) Griffin, J. M.; Forse, A. C.; Tsai, W. Y.; Taberna, P. L.; Simon, P.; Grey, C. P. *In Situ* NMR and Electrochemical Quartz Crystal Microbalance Techniques Reveal the Structure of the Electrical Double Layer in Supercapacitors. *Nat. Mater.* 2015, 14, 812−820.

(14) Prehal, C.; Weingarth, D.; Perre, E.; Lechner, R. T.; Amenitsch, H.; Paris, O.; Presser, V. Tracking the Structural Arrangement of Ions in Carbon Supercapacitor Nanopores Using *in situ* Small Angle X Ray Scattering. *Energy Environ. Sci.* 2015, 8, 1725−1735.

(15) Wang, H.; Köster, T. K. J.; Trease, N. M.; Ségalini, J.; Taberna, P. L.; Simon, P.; Gogotsi, Y.; Grey, C. P. Real Time NMR Studies of Electrochemical Double Layer Capacitors. *J. Am. Chem. Soc.* 2011, 133, 19270−19273.

(16) Deschamps, M.; Gilbert, E.; Azais, P.; Raymundo Piñero, E.; Ammar, M. R.; Simon, P.; Massiot, D.; Béguin, F. Exploring Electrolyte Organization in Supercapacitor Electrodes with Solid State NMR. *Nat. Mater.* 2013, 12, 351−358.

(17) Lee, K.; Yoon, Y.; Cho, Y.; Lee, S. M.; Shin, Y.; Lee, H.; Lee, H. Tunable Sub Nanopores of Graphene Flake Interlayers with Conductive Molecular Linkers for Supercapacitors. *ACS Nano* 2016, 10, 6799−6807.

(18) Yuan, K.; Xu, Y.; Uihlein, J.; Brunklaus, G.; Shi, L.; Heiderhoff, R.; Que, M.; Forster, M.; Chassé, T.; Pichler, T.; Riedl, T.; Chen, Y.; Scherf, U. Straightforward Generation of Pillared, Microporous Graphene Frameworks for Use in Supercapacitors. *Adv. Mater.* 2015, 27, 6714−6721.

(19) Raccichini, R.; Varzi, A.; Passerini, S.; Scrosati, B. The Role of Graphene for Electrochemical Energy Storage. *Nat. Mater.* 2015, 14, 271−279.

(20) Moon, I. K.; Lee, J.; Ruoff, R. S.; Lee, H. Reduced Graphene Oxide by Chemical Graphitization. *Nat. Commun.* 2010, 1, 73.

(21) Stoller, M. D.; Park, S.; Zhu, Y.; An, J.; Ruoff, R. S. Graphene Based Ultracapacitors. *Nano Lett.* 2008, 8, 3498−3502.

(22) Li, C.; Shi, G. Functional Gels Based on Chemically Modified Graphenes. *Adv. Mater.* 2014, 26, 3992−4012.

(23) Herrera Alonso, M.; Abdala, A. A.; McAllister, M. J.; Aksay, I. A.; Prud'homme, R. K. Intercalation and Stitching of Graphite Oxide with Diaminoalkanes. *Langmuir* 2007, 23, 10644−10649.

(24) Hung, W. S.; Tsou, C. H.; De Guzman, M.; An, Q. F.; Liu, Y. L.; Zhang, Y. M.; Hu, C. C.; Lee, K. R.; Lai, J. Y. Cross Linking with Diamine Monomers to Prepare Composite Graphene Oxide Frame work Membranes with Varying d Spacing. *Chem. Mater.* 2014, 26, 2983−2990.

(25) Banda, H.; Daffos, B.; Périé, S.; Chenavier, Y.; Dubois, L.; Aradilla, D.; Pouget, S.; Simon, P.; Crosnier, O.; Taberna, P. L.; Duclairoir, F. Ion Sieving Effects in Chemically Tuned Pillared Graphene Materials for Electrochemical Capacitors. *Chem. Mater.* 2018, 30, 3040−3047.

(26) Bourlinos, A. B.; Gournis, D.; Petridis, D.; Szabó, T.; Szeri, A.; Dékány, I. Graphite Oxide: Chemical Reduction to Graphite and Surface Modification with Primary Aliphatic Amines and Amino Acids. *Langmuir* 2003, 19, 6050−6055.

(27) Banda, H.; Périé, S.; Daffos, B.; Dubois, L.; Crosnier, O.; Simon, P.; Taberna, P. L.; Duclairoir, F. Investigation of Ion Transport in Chemically Tuned Pillared Graphene Materials through Electrochemical Impedance Analysis. *Electrochim. Acta* 2019, 296, 882−890.

(28) Srinivas, G.; Burress, J. W.; Ford, J.; Yildirim, T. Porous Graphene Oxide Frameworks: Synthesis and Gas Sorption Properties. *J. Mater. Chem.* 2011, 21, 11323−11329.

(29) Burress, J. W.; Gadipelli, S.; Ford, J.; Simmons, J. M.; Zhou, W.; Yildirim, T. Graphene Oxide Framework Materials: Theoretical Predictions and Experimental Results. *Angew. Chem., Int. Ed.* 2010, 49, 8902−8904.

(30) Salitra, G.; Soffer, A.; Eliad, L.; Cohen, Y.; Aurbach, D. Carbon Electrodes for Double Layer Capacitors I. Relations Between Ion and Pore Dimensions. *J. Electrochem. Soc.* 2000, 147, 2486−2493.

(31) Hummers, W. S.; Offeman, R. E. Preparation of Graphitic Oxide. *J. Am. Chem. Soc.* 1958, 80, 1339−1339.

(32) He, H.; Riedl, T.; Lerf, A.; Klinowski, J. Solid State NMR Studies of the Structure of Graphite Oxide. *J. Phys. Chem.* 1996, 100, 19954−19958.

(33) Cai, W.; Piner, R. D.; Stadermann, F. J.; Park, S.; Shaibat, M. A.; Ishii, Y.; Yang, D.; Velamakanni, A.; An, S. J.; Stoller, M.; An, J.; Chen, D.; Ruoff, R. S. Synthesis and Solid State NMR Structural

Characterization of 13C Labeled Graphite Oxide. *Science* **2008**, *321*, 1815−1817.

(34) Xu, Y.; Sheng, K.; Li, C.; Shi, G. Self Assembled Graphene Hydrogel *via* a One Step Hydrothermal Process. *ACS Nano* **2010**, *4*, 4324−4330.

(35) Vacchi, I. A.; Spinato, C.; Raya, J.; Bianco, A.; Ménard Moyon, C. Chemical Reactivity of Graphene Oxide towards Amines Elucidated by Solid State NMR. *Nanoscale* **2016**, *8*, 13714−13721.

(36) Freitas, J. C. C.; Emmerich, F. G.; Cernicchiaro, G. R. C.; Sampaio, L. C.; Bonagamba, T. J. Magnetic Susceptibility Effects on 13C MAS NMR Spectra of Carbon Materials and Graphite. *Solid State Nucl. Magn. Reson.* **2001**, *20*, 61−73.

(37) Szabó, T.; Berkesi, O.; Forgó, P.; Josepovits, K.; Sanakis, Y.; Petridis, D.; Dékány, I. Evolution of Surface Functional Groups in a Series of Progressively Oxidized Graphite Oxides. *Chem. Mater.* **2006**, *18*, 2740−2749.

(38) Hing, A. W.; Vega, S.; Schaefer, J. Transferred Echo Double Resonance NMR. *J. Magn. Reson. (1969 1992)* **1992**, *96*, 205−209.

(39) Jaroniec, C. P.; Filip, C.; Griffin, R. G. 3D TEDOR NMR Experiments for the Simultaneous Measurement of Multiple Carbon−Nitrogen Distances in Uniformly 13C,15N Labeled Solids. *J. Am. Chem. Soc.* **2002**, *124*, 10728−10742.

(40) Banda, H.; Aradilla, D.; Benayad, A.; Chenavier, Y.; Daffos, B.; Dubois, L.; Duclairoir, F. One Step Synthesis of Highly Reduced Graphene Hydrogels for High Power Supercapacitor Applications. *J. Power Sources* **2017**, *360*, 538−547.

(41) Stankovich, S.; Dikin, D. A.; Piner, R. D.; Kohlhaas, K. A.; Kleinhammes, A.; Jia, Y.; Wu, Y.; Nguyen, S. T.; Ruoff, R. S. Synthesis of Graphene Based Nanosheets *via* Chemical Reduction of Exfoliated Graphite Oxide. *Carbon* **2007**, *45*, 1558−1565.

(42) Brunauer, S.; Emmett, P. H.; Teller, E. Adsorption of Gases in Multimolecular Layers. *J. Am. Chem. Soc.* **1938**, *60*, 309−319.

(43) Jagiello, J.; Olivier, J. P. 2D NLDFT Adsorption Models for Carbon Slit Shaped Pores with Surface Energetical Heterogeneity and Geometrical Corrugation. *Carbon* **2013**, *55*, 70−80.

(44) Ue, M. Mobility and Ionic Association of Lithium and Quaternary Ammonium Salts in Propylene Carbonate and Γ Butyrolactone. *J. Electrochem. Soc.* **1994**, *141*, 3336−3342.

(45) Mysyk, R.; Raymundo Piñero, E.; Pernak, J.; Béguin, F. Confinement of Symmetric Tetraalkylammonium Ions in Nano porous Carbon Electrodes of Electric Double Layer Capacitors. *J. Phys. Chem. C* **2009**, *113*, 13443−13449.

(46) Lin, R.; Huang, P.; Ségalini, J.; Largeot, C.; Taberna, P. L.; Chmiola, J.; Gogotsi, Y.; Simon, P. Solvent Effect on the Ion Adsorption from Ionic Liquid Electrolyte into Sub Nanometer Carbon Pores. *Electrochim. Acta* **2009**, *54*, 7025−7032.

(47) Portet, C.; Taberna, P. L.; Simon, P.; Laberty Robert, C. Modification of Al Current Collector Surface by Sol−Gel Deposit for Carbon−Carbon Supercapacitor Applications. *Electrochim. Acta* **2004**, *49*, 905−912.

(48) de Levie, R. On Porous Electrodes in Electrolyte Solutions: I. Capacitance Effects. *Electrochim. Acta* **1963**, *8*, 751−780.

(49) Taberna, P. L.; Simon, P.; Fauvarque, J. F. Electrochemical Characteristics and Impedance Spectroscopy Studies of Carbon Carbon Supercapacitors. *J. Electrochem. Soc.* **2003**, *150*, A292−A300.

(50) Cole, K. S.; Cole, R. H. Dispersion and Absorption in Dielectrics I. Alternating Current Characteristics. *J. Chem. Phys.* **1941**, *9*, 341−351.

(51) Kondrat, S.; Wu, P.; Qiao, R.; Kornyshev, A. A. Accelerating Charging Dynamics in Subnanometre Pores. *Nat. Mater.* **2014**, *13*, 387−393.

(52) Tao, Y.; Xie, X.; Lv, W.; Tang, D. M.; Kong, D.; Huang, Z.; Nishihara, H.; Ishii, T.; Li, B.; Golberg, D.; Kang, F.; Kyotani, T.; Yang, Q. H. Towards Ultrahigh Volumetric Capacitance: Graphene Derived Highly Dense but Porous Carbons for Supercapacitors. *Sci. Rep.* **2013**, *3*, 2975.

(53) Liu, C.; Yan, X.; Hu, F.; Gao, G.; Wu, G.; Yang, X. Toward Superior Capacitive Energy Storage: Recent Advances in Pore Engineering for Dense Electrodes. *Adv. Mater.* **2018**, *30*, 1705713.

(54) Ashok Kumar, N.; Gambarelli, S.; Duclairoir, F.; Bidan, G.; Dubois, L. Synthesis of High Quality Reduced Graphene Oxide Nanosheets Free of Paramagnetic Metallic Impurities. *J. Mater. Chem. A* **2013**, *1*, 2789−2794.

Sparsely Pillared Graphene Materials for High Performance Supercapacitors: Improving Ion Transport and Storage Capacity

Harish Banda†, Sandy Périé†, Barbara Daffos¶‡, Pierre-Louis Taberna¶‡, Lionel Dubois†,

Olivier Crosnier¶§, Patrice Simon¶‡, Daniel Lee†, Gaël De Paëpe† and Florence Duclairoir†*

† Univ. Grenoble Alpes, CEA, CNRS, INAC, Grenoble, 38000, France.

‡ CIRIMAT, Université de Toulouse, CNRS, INPT, UPS, 31062 Toulouse, France.

§ Institut des matériaux Jean Rouxel (IMN), Université de Nantes, CNRS, Nantes, 44300,

France.

¶ Réseau sur le Stockage Electrochimique de l'Energie (RS2E), FR CNRS, 3459, France.

Graphene Oxide (GO) synthesis: GO synthesis was performed by following a modified Hummers and Offeman's method. [1-3] Graphite powder (3.1 g) was dispersed in H_2SO_4 (91 ml) under stirring into a 1 L beaker placed in an ice bath. $NaNO_3$ (1.5 g) was then added and the reaction media was stirred vigorously while maintaining the temperature under 2 °C. After 2 h, $KMnO_4$ (9 g) was added portion-wise to keep the mixture temperature below 4 °C. The reaction media was kept under stirring at such controlled temperature for a further 1 h, before it was let to reach room temperature. Then water (100 mL) was added slowly over a period of 20 minutes maintaining the temperature under 95 °C. The beaker was then placed into an oil bath and stirred at 95 °C. After 1.5 h, water (300 mL) was added, making sure the temperature did not rise above 85 °C. Stirring was continued for 1.5 h and then the reaction mixture was let to reach room temperature. H_2O_2 (30 mL) was added and the mixture was stirred for 1 h. Finally, water (450 mL) was added and the mixture was stirred overnight.

The mixture was then filtered through a P4 fritted Buchner filter (10-15 μm). The solid graphene oxide cake was re-dispersed in 600 mL of water, and the dispersion was homogenized under stirring for 1 h and sonication for a further hour. The mixture was then acidified with 100 ml of HCl and left under stirring overnight. Finally, the GO dispersion was filtered and centrifuged repeatedly until the supernatant reached pH 5. GO solution with a concentration of 5 mg.ml^{-1} was obtained by carefully measuring the weight of 10 ml of lyophilized GO.

Characterization techniques: The thermogravimetric analysis (TGA) of all samples were performed with Setaram TGA 92 at a heating ramp rate of 5 °C.min^{-1} from 30 °C to 800 °C under N_2 atmosphere. The crystallographic structures of the materials were determined by a wide-angle X-ray diffraction (XRD) system on a Panalytical X'pert PRO X-ray diffractometer using a Co Kα radiation source (λ=1.79 Å). X-ray photoelectron spectroscopy (XPS) analyses were performed

using a PHI Versa Probe II spectrometer with a monochromatized Al Kα X-ray source (1486.6 eV) focalized to a spot of 100 µm and with an electron take-off angle of $\theta = 45°$. Survey spectra of the photo-emitted electrons were recorded with a pass energy of 117 eV and the high-resolution spectra with a pass energy of 23.5 eV. The deconvolution of C 1s and N 1s core-level spectra was performed by fitting the individual components at values obtained from earlier reports by using Casa XPS software. Spectra were fitted into Gaussian-Lorentzian (30) shaped curves with full width at half maximum values kept under 1.5 in all cases. The morphology of the materials was characterized using a Zeiss Ultra 55 electron microscope at an accelerating voltage of 5 kV. Porosity characteristics were calculated from N_2 sorption isotherms measured at 77 K with Micromeritics ASAP 3020 porosimeter. Prior to the analysis samples were degassed under vacuum at 100 °C for 24 h. The adsorption isotherms were obtained and the specific surface area and the pore size distributions (PSD) were calculated by assuming a graphene-based structural framework and using a 2D non-local density functional theory (NLDFT) treatment of the fluid density in the pores, which are considered as energetically heterogeneous.[4] Electrical conductivity values were obtained from four-probe measurements using a Lucas Signatone QuadPro Resistivity system. Samples were prepared as thin films of ~ 100 µm by pressing under 10 T of pressure.

Solid-state nuclear magnetic resonance (ssNMR) spectroscopy was performed using a Bruker AVIII 400 MHz spectrometer equipped with 4 mm ambient-temperature and 3.2 mm low-temperature magic angle sample spinning (MAS) probes. $\{^1H-\}^{13}C$ and $\{^1H-\}^{15}N$ cross-polarization (CP)MAS experiments[5] were recorded using 100 kHz nutation for ^1H π/2 pulses and SPINAL-64[6] heteronuclear decoupling, a ramped (50-100%) power to match a Hartmann-Hahn CP condition when using 50 kHz for ^{13}C or ^{15}N nutation during 2 ms CP spin-locking and using a spin-echo of two rotor periods total duration (50 kHz for ^{13}C or ^{15}N π-pulses) before free-induction

decay (FID) acquisition. A minimum of 8192 and 4096 transients were recorded for the {^{1}H-}^{13}C and {^{1}H-}^{15}N CPMAS experiments, respectively, using a recycle delay of 0.5 s between transients and 250 Hz exponential apodization before Fourier transformation of the FID. The 2D *z*-filtered TEDOR[7,8] ^{15}N–^{13}C dipolar correlation spectrum was recorded with a starting {^{1}H-}^{13}C CP step of 2 ms, 1.3 ms total TEDOR mixing (to ensure correlation peaks are only from bonded ^{15}N–^{13}C pairs), 6400 transients for each of 16 complex (States-TPPI) t_1 increments of 123.35 μs, using a recycle delay of 0.5 s between transients and 250 Hz exponential apodization in both dimensions before double Fourier transform.

Electrochemical analysis: The synthesized materials were first tested in a three-electrode supercapacitor configuration with porous carbon (YP50) as counter, silver wire as reference electrodes, and a 25 μm thick cellulose sheet as a separator. Large porous carbon electrodes with excess weight were used to counter the charges and ensure distinct responses from the working electrodes. A custom-built Swagelok type cell was used to assemble the cell components. The working electrodes were fabricated as a slurry by mixing active materials, polyvinylidene fluoride (PVDF), and acetylene black carbon in a ratio of 80:10:10 using N-methyl-2-pyrrolidone and were coated onto 0.5 cm^2 stainless steel disks. The as-prepared electrodes were dried at 65 ^{o}C in air for 3 h prior to drying under vacuum at 120 ^{o}C overnight. The dried electrodes were noted to weigh 1 -1.5 mg, resulting in loading densities of 2-3 mg.cm^{-2}. 1M tetralkylammonium tetrafluoroborate (TAABF$_4$) salt solutions in anhydrous acetonitrile with varying cations; ethyl (TEABF$_4$), propyl (TPABF$_4$), butyl (TBABF$_4$) and hexyl (THABF$_4$) were used as electrolytes. The performances of the SCs were evaluated using cyclic voltammetry (CV) at various scan rates. A multichannel VMP3 potentiostat/galvanostat with EC-Lab software (Biologic) was used for all electrochemical techniques. CV measurements were performed between - 1 to 1 V *vs.* Ag. at scan rates of 0.001-1

V.s^{-1}. The gravimetric capacitances (C) were derived from CV curves using the equation C = (∫ I(v).dv) /(m(dv/dt).V). ∫ I(v).dv is the total area under the curve in the potential window, dv/dt is the scan rate, m is the mass of the active material in the working electrode and V is the total potential window. Two-electrode CVs were performed using equal weights of active materials in both electrodes and tested in a 0-2.8 V range at scan rates of 0.001-1 V.s^{-1}.

Material	TGA analyses	XPS - Elemental Composition			XRD analyses		Gas Sorption analyses
	Wt. loss (%)	C %	O %	N %	d (Å) - G	d (Å) – CL	SSA (m^2.g^{-1})
GO	43	74.7	25.3	-	-	7.6	-
RGO	14	91.2	4.5	4.3	3.7	-	330
6 RP 1	34	88.3	5.6	6.3	3.9	7.8	138
6 RP 02	24	87.4	6.3	6.2	3.9	7.6	201
6 GH 005	26	89.3	5.7	5.0	3.9	7.9	206
6 GH 005 AD	27	89.1	5.8	5.1	3.9	7.8	148

Table S1. Thermal gravimetric weight loss values, elemental composition values from X-ray photoelectron spectroscopy, d-spacing obtained from X-ray diffraction spectra, and specific surface area values obtained from N$_2$ gas sorption analyses for the synthesized materials.

Material	f_0 under +1 V *vs.* Ag (Hz)	Positive Time Constant (s)	f_0 under -1 V *vs.* Ag (Hz)	Negative Time Constant (s)
RGO	0.187	5.4	0.187	5.4
6 RP 1	0.078	12.8	0.058	17.3
6 RP 02	0.187	5.4	0.187	5.4
6 GH 005	0.140	7.1	0.140	7.1

Table S2. The imaginary part of the capacitance goes through a maximum at f_0 and is identified from the imaginary capacitance *vs.* frequency plot. Time constant (τ_0) values of the synthesized materials were extracted from the f_0 values under both positive and negative polarizations *vs.* Ag.

Material	Electrolyte / Voltage (V)	Scan rate or Current density	Specific Capacitance $(F.g^{-1})$	Specific Capacitance $(F.cm^{-3})$	Ref
Activated Carbon	1 M EMIBF$_4$ (3.5 V)	1 A.g^{-1}	207	104	9
CDC	EMITFSI (3.0 V)	0.3 A.g^{-1}	160	85	10
MHCN	1 M EMIBF$_4$ (2.5 V)	0.5 A.g^{-1}	103	80	11
CCNC	1 M EMIBF$_4$ (4.0 V)	1 A.g^{-1}	156	206	12
EM-CCG	1 M EMIBF$_4$ (3.5 V)	0.1 A.g^{-1}	209	261	13
Graphene/SWNT film	1 M EMIBF$_4$ (4.0 V)	0.5 A.g^{-1}	199	211	14
HGF	1 M EMIBF$_4$ (3.5 V)	1 A.g^{-1}	298	212	15
HPGM	1 M TEABF$_4$ (2.5 V)	0.1 A.g^{-1}	108	171	16
Porous carbon	1.5 TEABF$_4$ (2.54 V)	0.002 V.s^{-1}	156	145	17
Compressed-aMEGO	1 M EMIMBF$_4$ (3.5 V)	0.1 V.s^{-1}	147	110	18
6 GH 0.05 AD	1 M TEABF$_4$ (2.8 V)	0.01 V.s^{-1}	190	210	This work
		0.1 V.s^{-1}	159	175	
		1 V.s^{-1}	81	90	

Table S3. Comparison of the tested materials with reports in literature in symmetrical SCs.
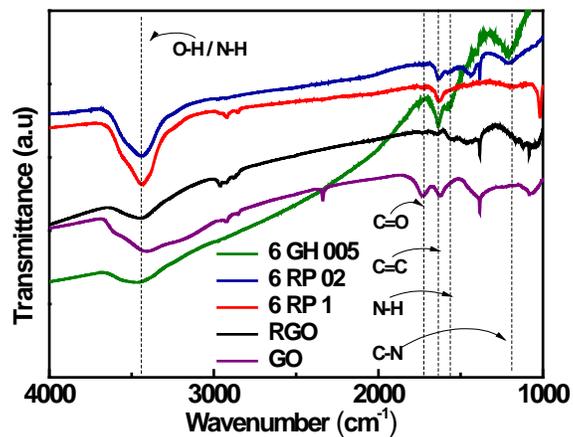
Figure S1. FTIR spectra of the precursor (GO), pillared graphene materials (RPs/GHs) and reduced graphene oxide (RGO) indicate reduction of C=O functionalities and appearance of the N-H and C-N bonds for RP/GH samples are observed.
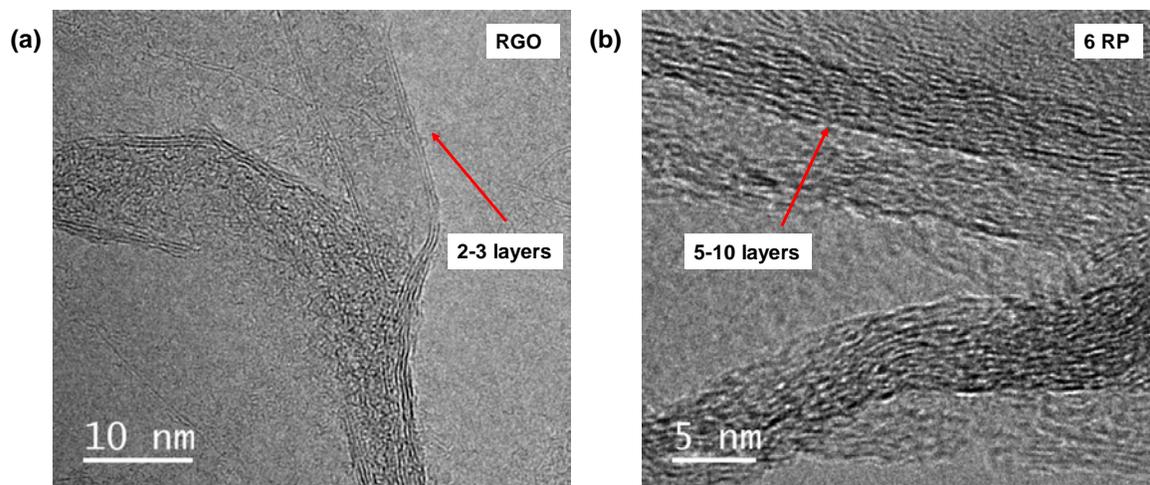
Figure S2. (a) RGO displays ordered graphene sheets whereas the sheets in (b) 6 RP appear rugose, probably due to the functionalization by diamines.
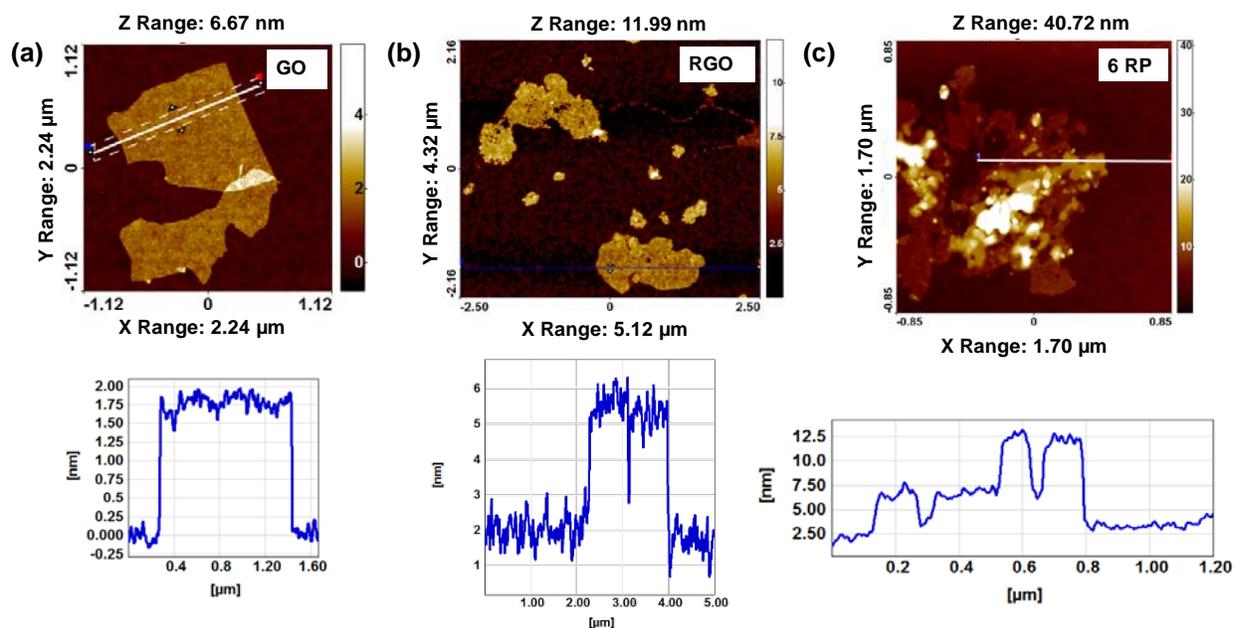
Figure S3. The Atomic Force Microscopy (AFM) analyses of (a) GO, (b) RGO and (c) 6 RP show clear differences in height profiles. The cross-linking of graphene sheets leads to growth of particle sizes in the Z direction and the elevated height profile of 6 RP in AFM compared to RGO confirms the pillaring of sheets.
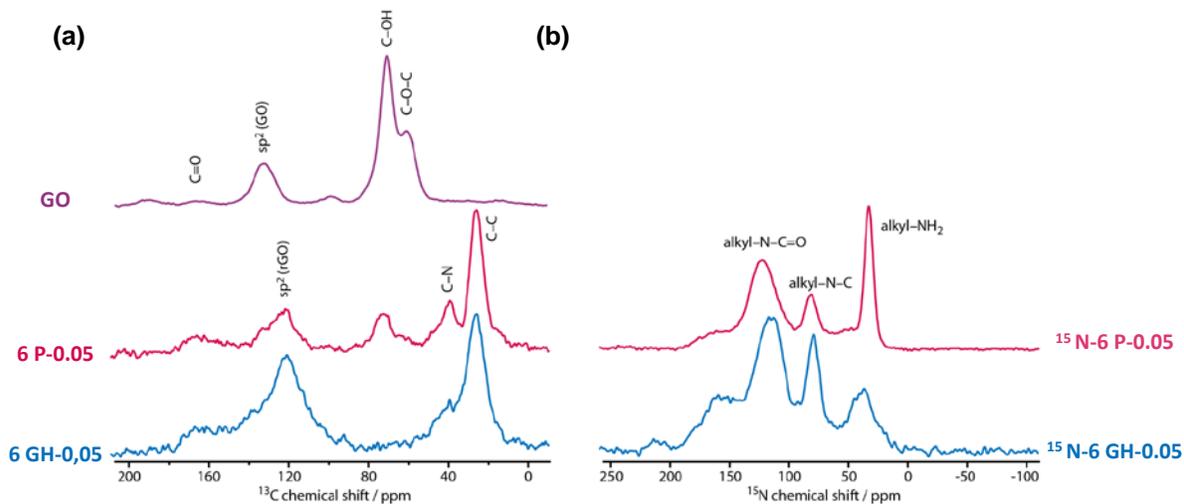
Figure S4. Solid-state magic angle spinning (MAS) NMR spectra recorded at 9.4 T (^{1}H Larmor frequency of 400 MHz), 300 K, and using a MAS frequency of 12 kHz. (a) {^{1}H-}^{13}C CP spectra (natural isotopic abundance) of graphene oxide (GO), unreduced pillared material (6-P-0.05), and pillared graphene hydrogel (6-GH-0.05). (b) {^{1}H-}^{15}N CP spectra of unreduced pillared material (6-P-0.05) and pillared graphene hydrogel (6-GH-0.05) synthesized with ^{15}N-labelled 1,6-diaminohexane.
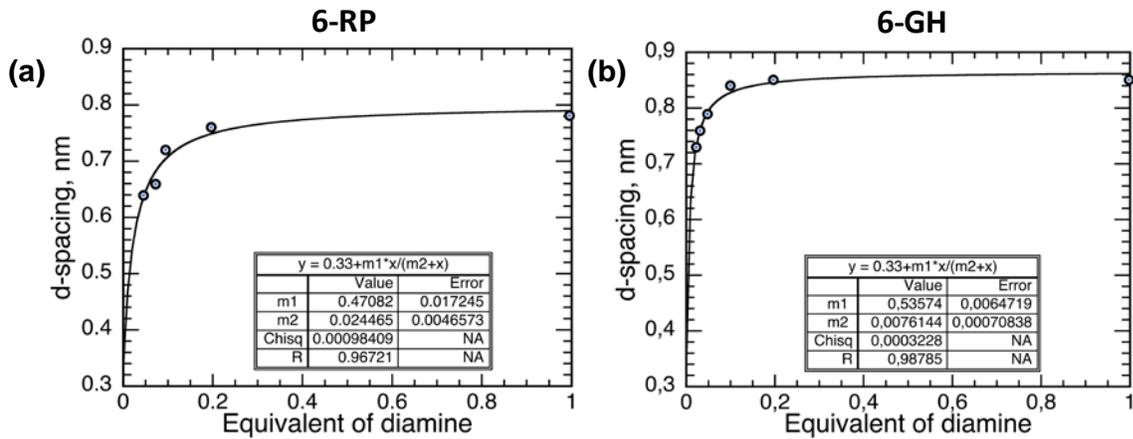
Figure S5. Variation of d-spacing values with equivalents in (a) 6-RP and (b) 6-GH. Fitting to Langmuir's chemisorption isotherm shows a good match. Saturation of d-spacing values at higher equivalents suggests grafting instead of physical sorption on the surface.
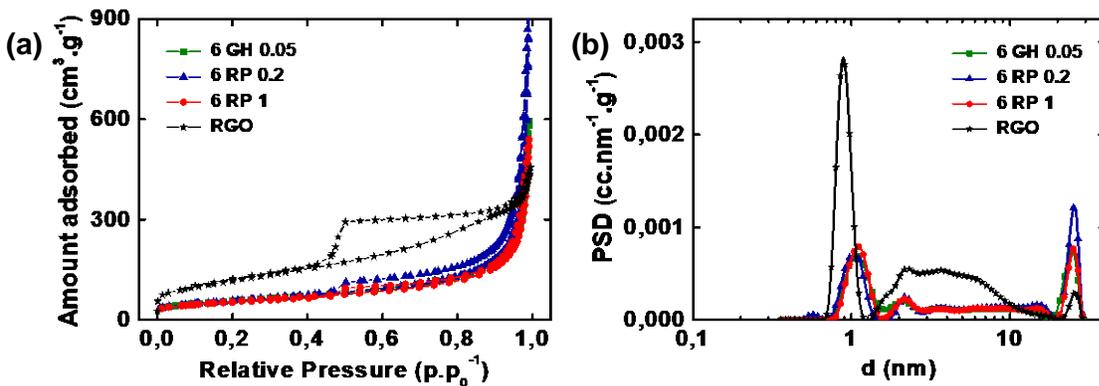
Figure S6. (a) N_2 sorption isotherms recorded at 77 K and (b) pore size distributions calculated using 2D non-local density functional theory for the synthesized materials.
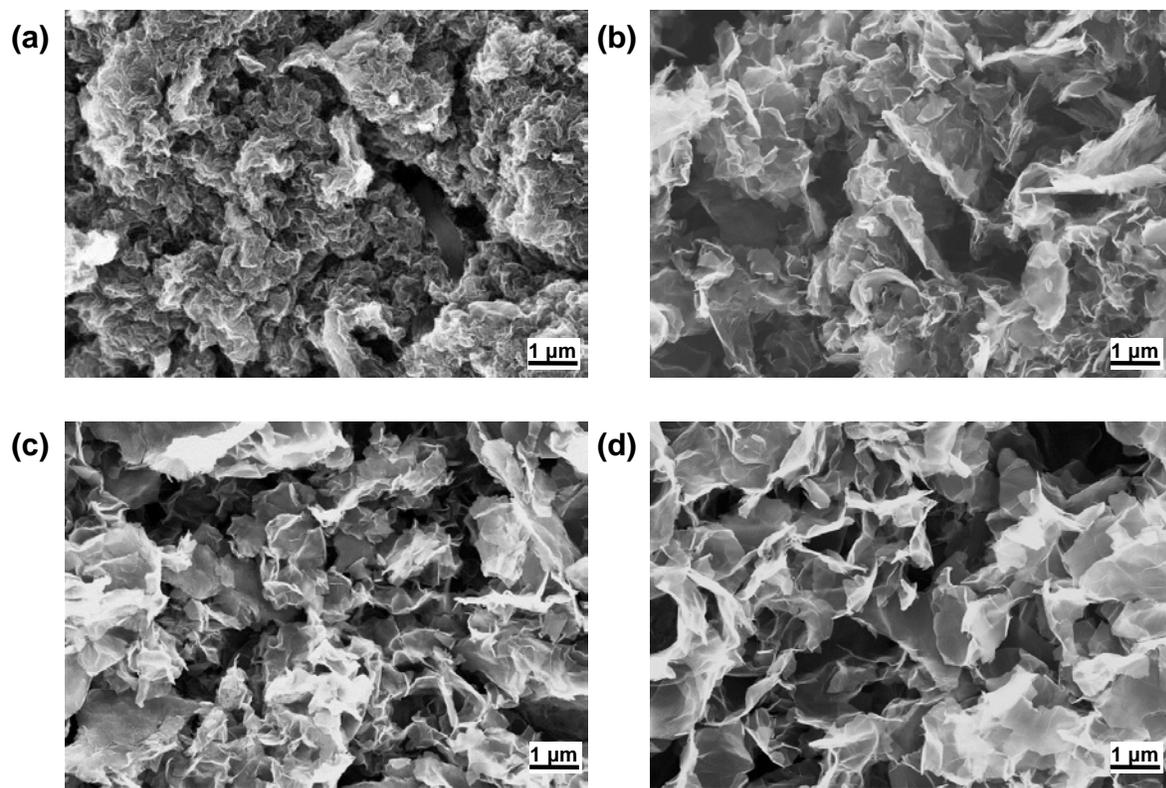
Figure S7. Scanning electron microscopy images of (a) RGO, (b) 6-RP-1, (c) 6-RP-0.2, and (d) 6-GH-0.05.
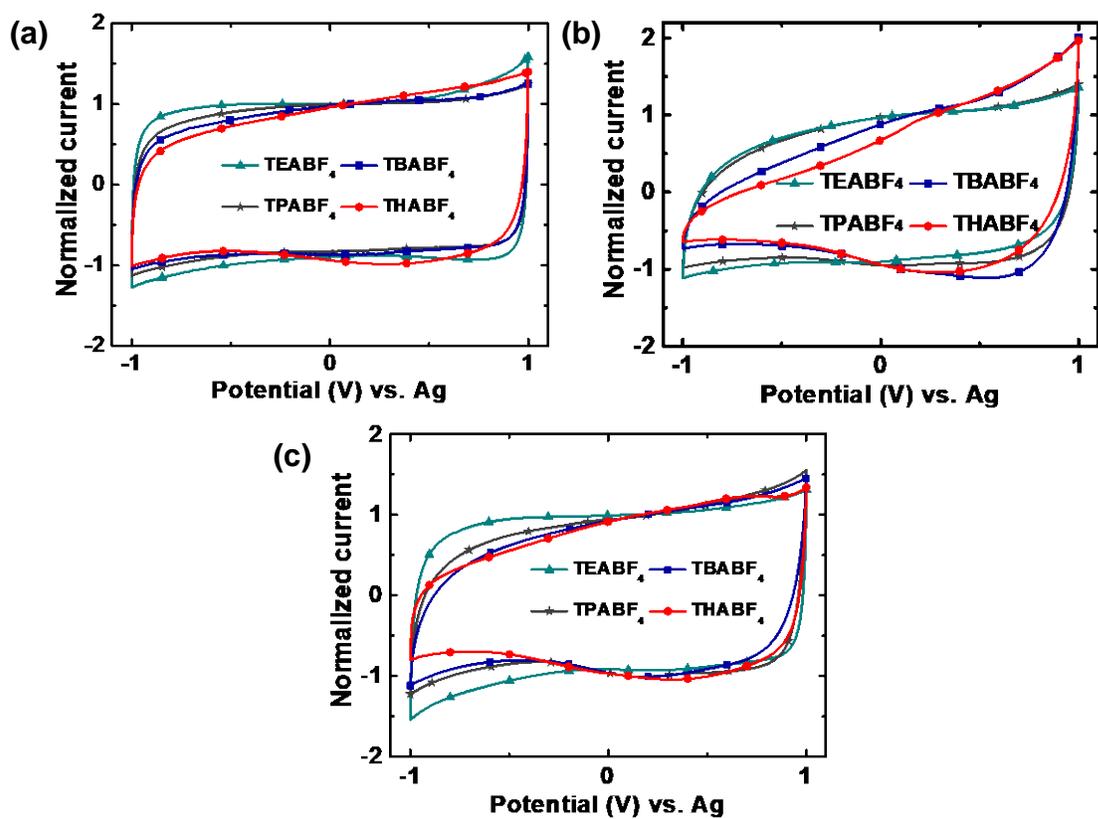
Figure S8. Normalized three-electrode cyclic voltammograms of (a) RGO, (b) 6-RP-1, and (c) 6-RP-0.2, obtained at a scan rate of 0.02 V.s^{-1} in the voltage range of -1 V to 1 V *vs.* Ag in 1 M solutions of TAABF$_4$ salts in acetonitrile (AN).
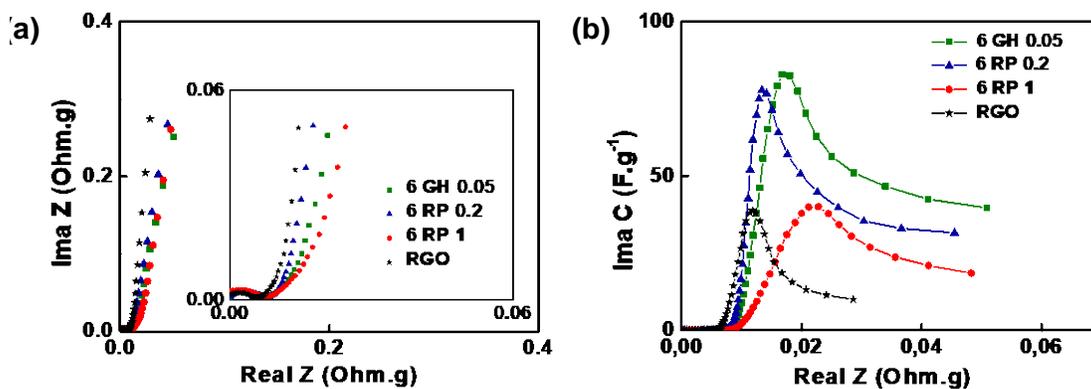
**Figure S9.** Electrochemical impedance measurements and CVs performed on the synthesized materials in a three-electrode configuration using 1 M TEABF$_4$/AN as electrolyte. (a) Normalized Nyquist plots obtained at 1 V *vs.* Ag. A zoom of the high and mid-frequency regions in Nyquist plots is shown in the insets. (b) Imaginary capacitance vs real impedance plots at 1 V *vs.* Ag.
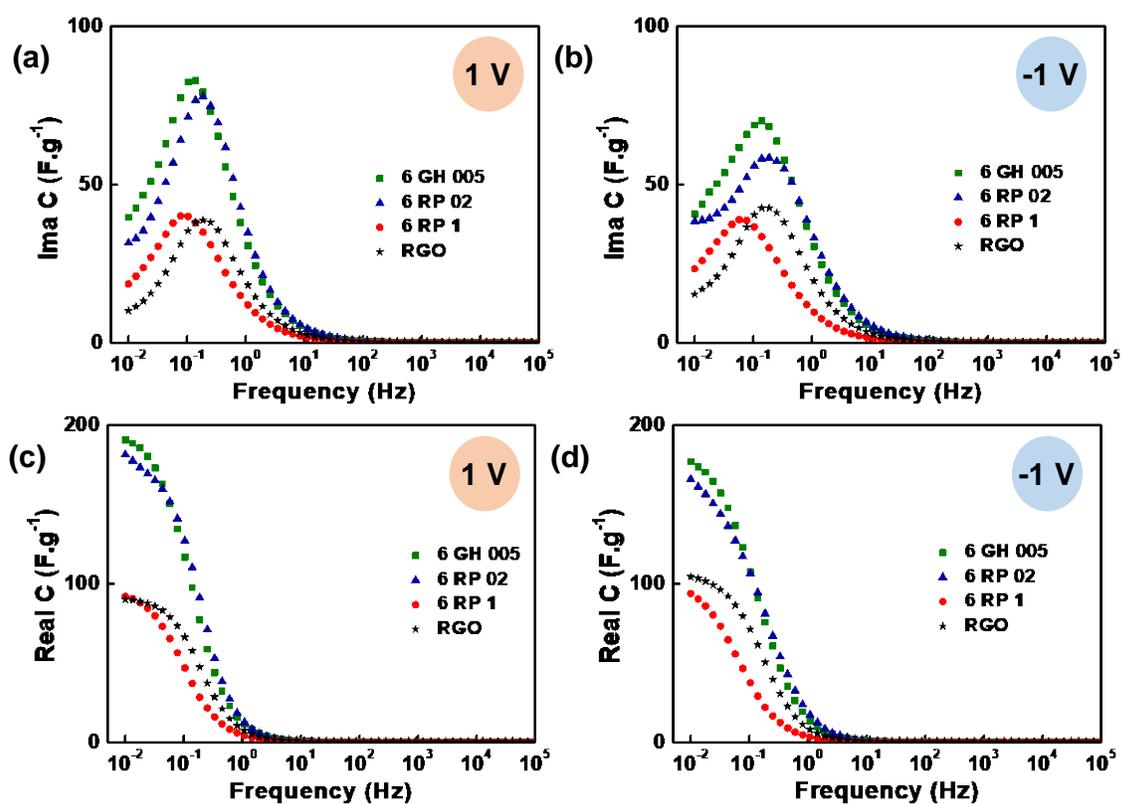
Figure S10. Imaginary capacitance vs. frequency plots for the synthesized materials in 1 M TEABF$_4$/AN electrolyte at 1 V (a) and -1 V (b) *vs.* Ag. Real capacitance vs. frequency plots at 1 V (c) and -1 V (d) *vs.* Ag.
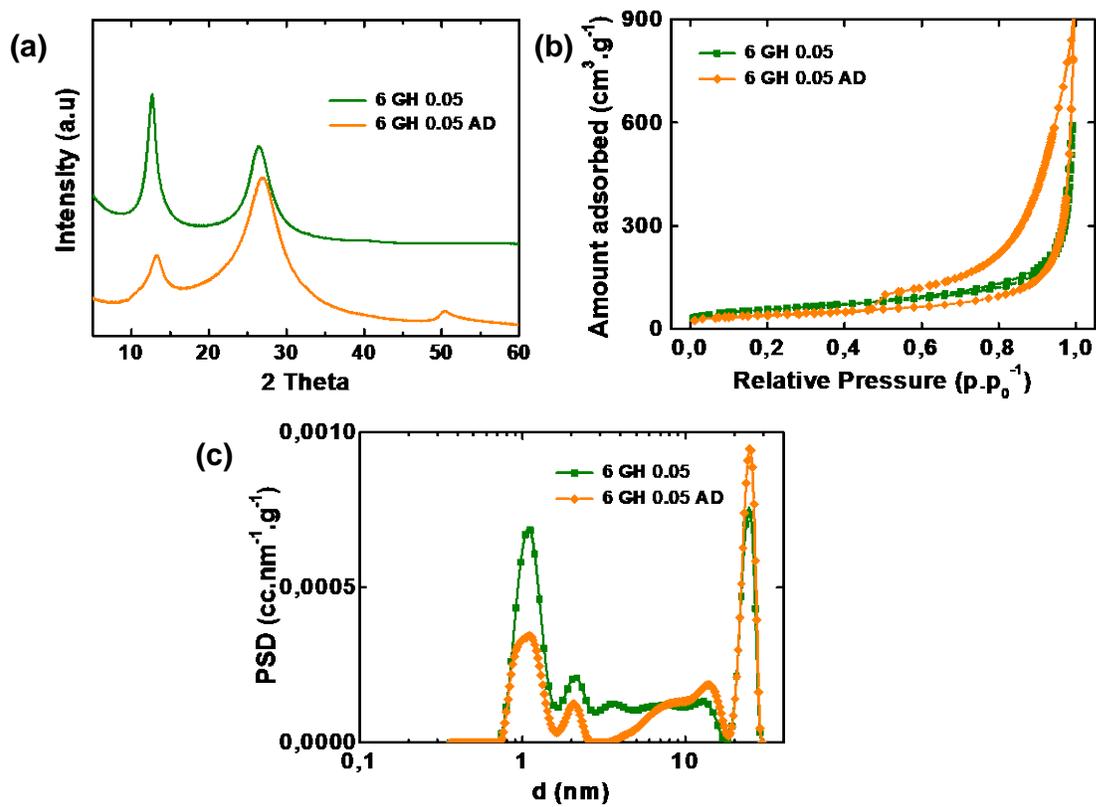
Figure S11. (a) X-Ray diffraction patterns, (b) N_2 gas sorption isotherms, and (c) pore size distributions of 6-GH-0.05 and 6-GH-0.05-AD.
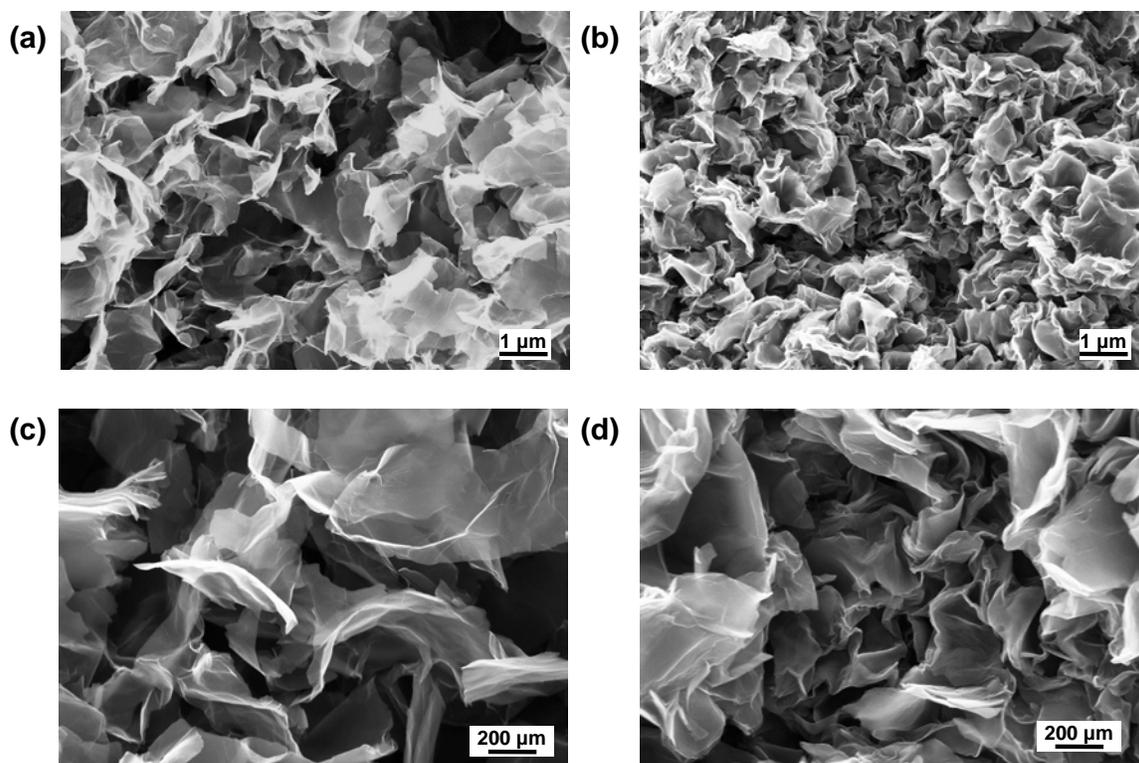
Figure S12. Scanning electron microscopy images of (a,c) freeze dried 6-GH-0.05 and (c,d) air dried 6-GH-0.05-AD under different magnifications.
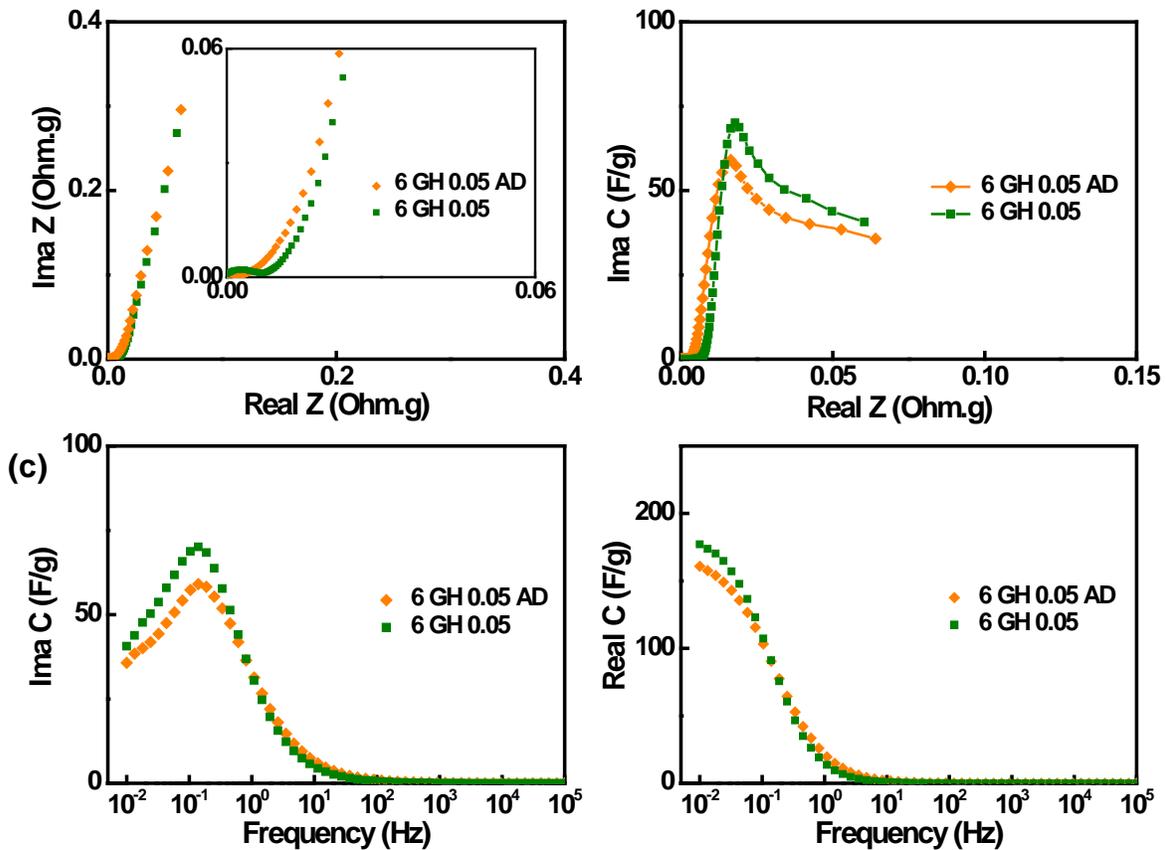
Figure S13. (a) Normalized Nyquist plots, (b) Ima C *vs.* Real Z, (c) Ima C *vs.* frequency and (d) Real C *vs.* frequency plots obtained at -1 V *vs.* Ag for 6 GH-0.05 and its dense counterpart 6 GH-0.05 AD. τ_0 values of 6 GH-1, 6 GH-0.05 and 6 GH -0.05 AD quantify the overall differences in ion transport for the materials. R_i values for 6 GH-1, 6 GH-0.05 and 6 GH -0.05 AD were found to be 57, 13 and 15 mOhm.g respectively.
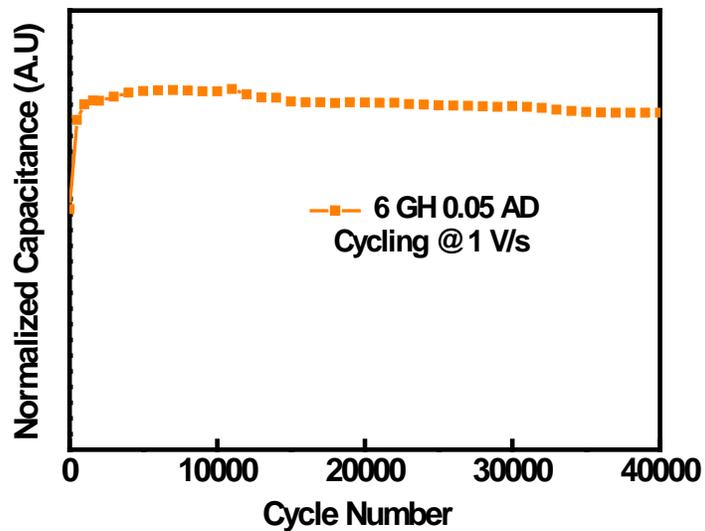
Figure S14. Cycling 6-GH-0.05-AD at a high rate of 1 V.s^{-1} in 0 - 2.8 V using 1 M TEABF$_4$/AN electrolyte for 40000 cycles.
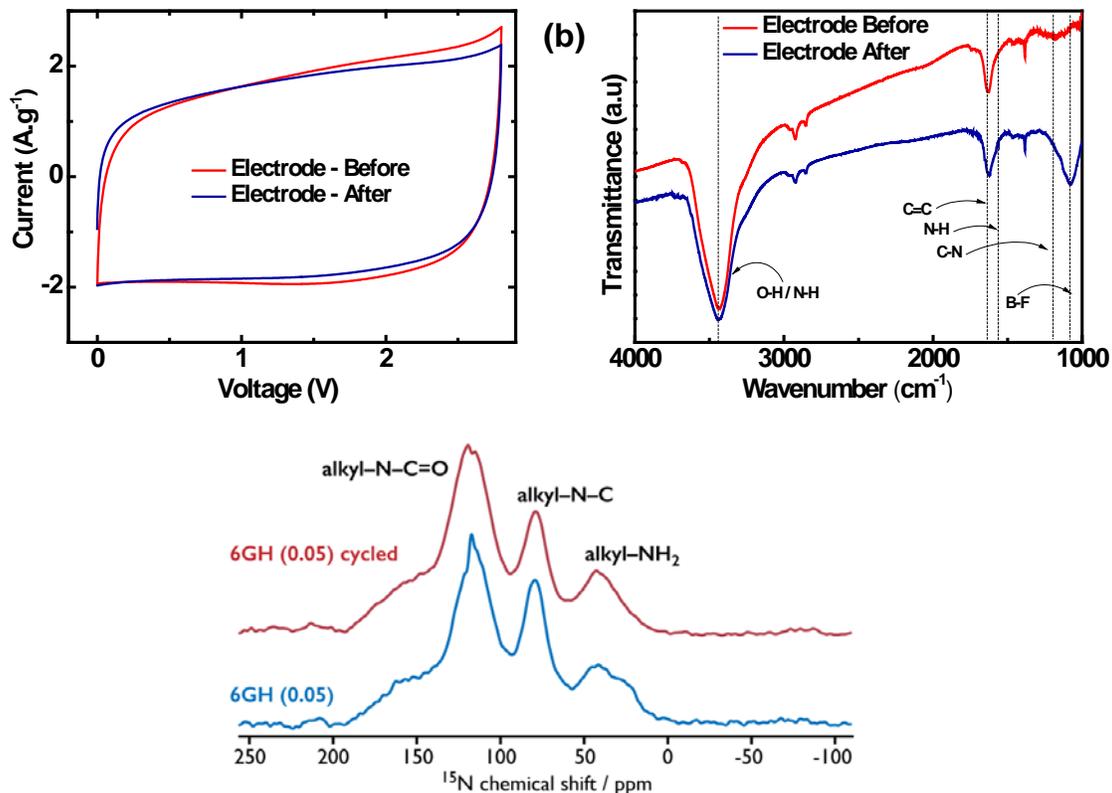
Figure S15. (a) Cyclic Voltammetry (CV) curves of the 6 GH 0.05 AD electrode at 5th and 1000th cycles in 1 M TEABF$_4$/AN at a scan rate of 50 mV/s in a two-electrode configuration. Minor losses in the currents are observed over the cycling. (b) The Fourier Transform Infrared Spectra of the 6 GH 0.05 AD electrode shows the presence of similar peaks before and after cycling. An additional peak corresponding to the BF$_4$ anions (~1100 cm^{-1}) could also be seen in the cycled electrode. (c) ^{15}N Nuclear Magnetic Resonance analysis confirms that the N atoms in the 6 GH 0.05 AD electrode remain unaltered upon cycling.
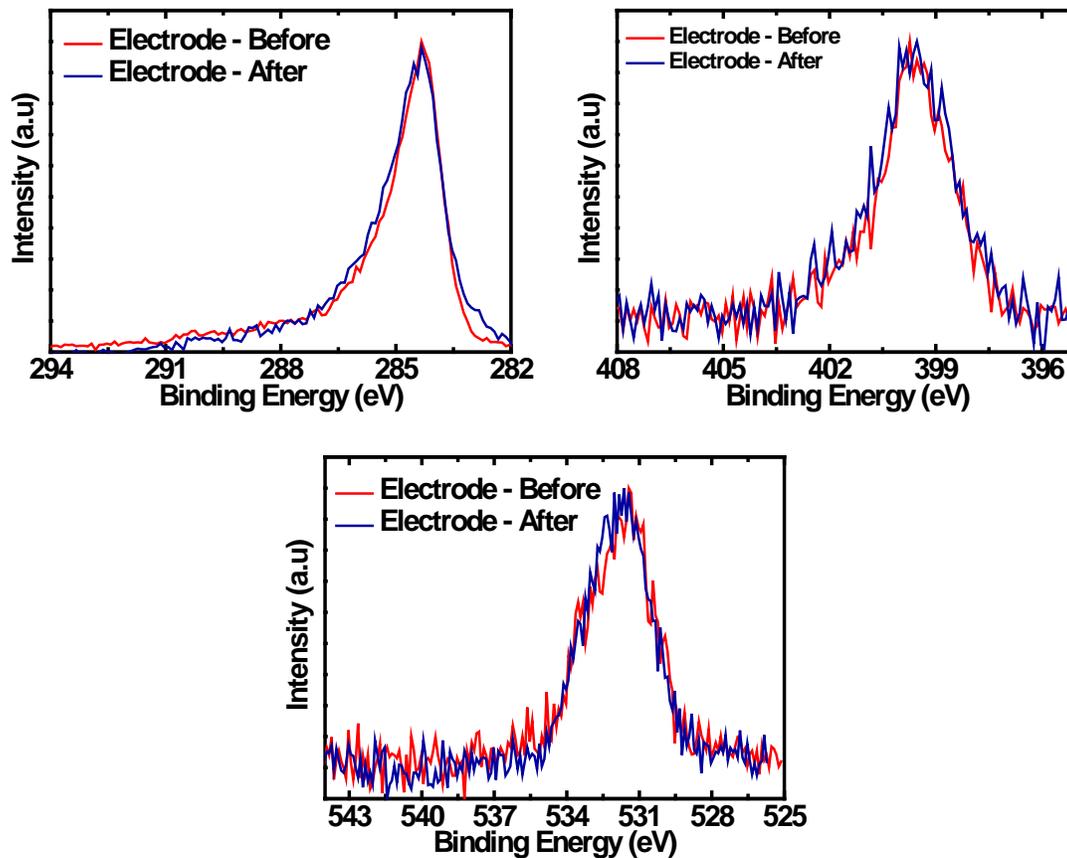
Figure S16. The (a) C 1s, (b) N 1s and (c) O 1s high resolution X-ray photoelectron spectra of the 6 GH 0.05 AD electrode suggest similar surface chemical composition of the material before and after cycling.

REFERENCES

(1) Hummers, W. S.; Offeman, R. E. Preparation of Graphitic Oxide. J. Am. Chem. Soc. 1958, 80, 1339–1339.

(2) Banda, H.; Aradilla, D.; Benayad, A.; Chenavier, Y.; Daffos, B.; Dubois, L.; Duclairoir, F. One-Step Synthesis of Highly Reduced Graphene Hydrogels for High Power Supercapacitor Applications. J. Power Sources 2017, 360, 538–547.

(3) Ashok Kumar, N.; Gambarelli, S.; Duclairoir, F.; Bidan, G.; Dubois, L. Synthesis of High Quality Reduced Graphene Oxide Nanosheets Free of Paramagnetic Metallic Impurities. J. Mater. Chem. A 2013, 1, 2789–2794.

(4) Jagiello, J.; Olivier, J. P. 2D-NLDFT Adsorption Models for Carbon Slit-Shaped Pores with Surface Energetical Heterogeneity and Geometrical Corrugation. Carbon 2013, 55, 70–80.

(5) Fung, B. M.; Khitrin, A. K.; Ermolaev, K. An Improved Broadband Decoupling Sequence for Liquid Crystals and Solids. J. Magn. Reson. 2000, 142, 97–101.

(6) Schaefer, J.; Stejskal, E. O. Carbon-13 Nuclear Magnetic Resonance of Polymers Spinning at the Magic Angle. J. Am. Chem. Soc. 1976, 98, 1031–1032.

(7) Jaroniec, C. P.; Filip, C.; Griffin, R. G. 3D TEDOR NMR Experiments for the Simultaneous Measurement of Multiple Carbon−Nitrogen Distances in Uniformly 13C,15N-Labeled Solids. J. Am. Chem. Soc. 2002, 124, 10728–10742.

(8) Hing, A. W.; Vega, S.; Schaefer, J. Transferred-Echo Double-Resonance NMR. J. Magn. Reson. 1969 1992, 96, 205–209.

(9)   Alonso, A.; Ruiz, V.; Blanco, C.; Santamaría, R.; Granda, M.; Menéndez, R.; de Jager, S. G. E. Activated Carbon Produced from Sasol-Lurgi Gasifier Pitch and Its Application as Electrodes in Supercapacitors. Carbon 2006, 44, 441–446.

(10) Largeot, C.; Portet, C.; Chmiola, J.; Taberna, P.-L.; Gogotsi, Y.; Simon, P. Relation between the Ion Size and Pore Size for an Electric Double-Layer Capacitor. J. Am. Chem. Soc. 2008, 130, 2730–2731.

(11) Hao, G.-P.; Lu, A.-H.; Dong, W.; Jin, Z.-Y.; Zhang, X.-Q.; Zhang, J.-T.; Li, W.-C. Sandwich-Type Microporous Carbon Nanosheets for Enhanced Supercapacitor Performance. Adv. Energy Mater. 2013, 3, 1421–1427.

(12) Bu, Y.; Sun, T.; Cai, Y.; Du, L.; Zhuo, O.; Yang, L.; Wu, Q.; Wang, X.; Hu, Z. Compressing Carbon Nanocages by Capillarity for Optimizing Porous Structures toward Ultrahigh-Volumetric-Performance Supercapacitors. Adv. Mater. 2017, 29, 1700470.

(13) Yang, X.; Cheng, C.; Wang, Y.; Qiu, L.; Li, D. Liquid-Mediated Dense Integration of Graphene Materials for Compact Capacitive Energy Storage. Science 2013, 341, 534.

(14) Pham, D. T.; Lee, T. H.; Luong, D. H.; Yao, F.; Ghosh, A.; Le, V. T.; Kim, T. H.; Li, B.; Chang, J.; Lee, Y. H. Carbon Nanotube-Bridged Graphene 3D Building Blocks for Ultrafast Compact Supercapacitors. ACS Nano 2015, 9, 2018–2027.

(15) Xu, Y.; Lin, Z.; Zhong, X.; Huang, X.; Weiss, N. O.; Huang, Y.; Duan, X. Holey Graphene Frameworks for Highly Efficient Capacitive Energy Storage. Nat. Commun. 2014, 5, 4554.

(16) Tao, Y.; Xie, X.; Lv, W.; Tang, D.-M.; Kong, D.; Huang, Z.; Nishihara, H.; Ishii, T.; Li, B.; Golberg, D.; Kang, F.; Kyotani, T.; Yang, Q. H. Towards Ultrahigh Volumetric Capacitance: Graphene Derived Highly Dense but Porous Carbons for Supercapacitors. Sci. Rep. 2013, 3, 2975.

(17) Wang, H.; Gao, Q.; Hu, J.; Chen, Z. High Performance of Nanoporous Carbon in Cryogenic Hydrogen Storage and Electrochemical Capacitance. Carbon 2009, 47, 2259–2268.

(18) Murali, S.; Quarles, N.; Zhang, L. L.; Potts, J. R.; Tan, Z.; Lu, Y.; Zhu, Y.; Ruoff, R. S. Volumetric Capacitance of Compressed Activated Microwave-Expanded Graphite Oxide (a-MEGO) Electrodes. Nano Energy 2013, 2, 764–768.